Discrete Ordinate Theory of Radiative Transfer

II. Scattering from Maritime Haze

By George W. Kattawar, Gilbert N. Plass, and Frances E. Catchings

The research described in this report was

funded by the

National Aeronautics and Space Administration

Contract No. NGR 44-001-117

Department of Physics
Texas A&M University
College Station, Texas 77843

December 3, 1971

A paper based on the material in this report has been submitted to the Journal of Atmospheric Sciences.

Discrete Ordinate Theory of Radiative Transfer
II. Scattering from Maritime Haze

George W. Kattawar, Gilbert N. Plass, and Frances E. Catchings

Department of Physics, Texas A&M University, College Station, Texas 77840

ABSTRACT

Discrete ordinate theory is used to calculate the reflected and transmitted radiance of photons which have interacted with plane-parallel maritime haze layers. The results are presented for three solar zenith angles, three values of the surface albedo, and a range of optical thicknesses from very thin to very thick. The diffuse flux at the lower boundary and the cloud albedo are tabulated. The forward peak and other features in the single scattered phase function cause the radiance in many cases to be very different from that for Rayleigh scattering. In particular the variation of the radiance with both the zenith or nadir angle and the azimuthal angle is more marked and the relative limb darkening under very thick layers is greater for haze M than for Rayleigh scattering. The downward diffuse flux at the lower boundary for A = 0 is always greater and the cloud albedo is always less for haze M than for Rayleigh layers.

1. Introduction

Discrete ordinate theory is an entirely rigorous method for the solution of the equations for radiative transfer. The general theory has been presented by Preisendorfer (1965), while important contributions to the theory have been made by Twomey et al (1966) and more recently by Grant and Hunt (1969). Plass, Kattawar and Catchings (1972) (referred to hereafter as I) in the first paper in this series have presented the theory in a particularly simple and improved form designed for physical applications. The theory given in our papers has the following important advantages: 1. calculations can readily be made for large optical depths and with highly anisotropic phase functions; 2. all orders of multiple scattering are calculated at once with a corresponding reduction in computer time over methods involving iterations; 3. layers of any thickness may be combined, so that a realistic model of the atmosphere may be developed from any arbitrary number of layers (the thickness of each layer as well as its optical properties may be chosen without regard to the properties of the other layers); 4. results are obtained for any desired value of the surface albedo (including the value unity) as well as for any polar angle which corresponds to one of the set given by the Lobatto integration scheme for the number of integration points chosen (the polar angle $\theta = 0°$ is always included in the set); 5. all fundamental equations can be interpreted immediately in terms of the physical interactions appropriate to the problem.

In this paper we present the results of calculations of the upward and downward radiance for scattering from maritime hazes of various optical thicknesses and with various ground albedos. The haze M model proposed by Deirmendjian (1969) is used. The number of particles with a given

radius is proportional to $r \exp(-8.944\ r^{\frac{1}{2}})$, where r is the particle radius. The mode radius or size of maximum frequency in the distribution is 0.05 μ. The single scattering phase function is calculated assuming a wavelength of 0.75 μ and a real index of refraction of 1.34 from Mie theory by the method described by Kattawar and Plass (1967). A Lambert surface is assumed in these discrete ordinate calculations with a surface albedo A. The single scattering albedo of the haze droplets is taken as unity.

Results for a maritime haze previously reported in the literature include: Kattawar and Plass (1968), upward and downward radiance calculated by a Monte Carlo method for $\mu_0 = 0.1$ and 1, A = 0 and 1, $\tau = 0.01$, 1, and 10; Hansen (1969), upward radiance only calculated by the doubling method for all values of μ_o, A = 0, $\tau = 0.5$ to 32; Dave and Gazdag (1970), upward and downward radiance calculated by the successive scattering iterative method for $\mu_o = 0.5$, A = 0, $\tau = 0.1$ to 1, where μ_o is the cosine of the angle between the vertical and the direction of the incident radiation.

2. Computational Aspects

The phase function for the haze m model was evaluated at every 2° interval starting at 0°. This function was then decomposed into a Fourier expansion, i.e.,

$$p(\cos\Theta) = \sum_{\ell=0}^{N} p_\ell(\mu,\mu') \cos\ell(\phi-\phi') \tag{1}$$

where the limit of the summation N is a function of μ and μ' for a desired degree of accuracy. The reason for this functional dependence follows from the expression

$$\cos\Theta = \mu\,\mu' + \sqrt{1-\mu^2}\ \sqrt{1-\mu'^2}\ \cos(\phi-\phi'); \tag{2}$$

different portions of the phase function curve are covered as $\cos(\phi-\phi')$ varies between ±1 for different values of μ and μ'. This dependence was first investigated by Dave and Gazdag (1970).

For the discrete ordinate representation the values for μ and μ' are obtained from the abscissa of a Lobatto integration, which fits a phase function of 81st degree exactly. The maximum value of N used in Eq. (1) was 89 for $\mu = \mu' = 0.0378$. The criterion used to truncate the series was that the number of terms $p_\ell(\mu_i,\mu_j)$ (see Eq. (28) of I) used in Eq. (1) should be sufficient to fit the original phase function to at least 1% for $\phi-\phi' = 0°$, 30°, 60°, 90°, 120°, 150° and 180°.

It was found that the error vector namely

$$\varepsilon_j = \sum_{i=1}^{n} (p_o(\mu_i,\mu_j)C_i) - (2\pi)^{-1},\ j = 1, 2, , , , , , m,$$

where for this particular case n = 42 and m = 21 was only a few hundredths of a percent of the normalization constant. From this correction vector $\underset{\sim}{\varepsilon}$ a small symmetric correction matrix was generated which was added to the $p_o(\mu_i,\mu_j)$ to insure normalization to full machine accuracy. The modified single scattering phase function is shown in Fig. 1. This is the actual phase function used in the calculation. It was generated by using Eq. (1) for the renormalized $p_o(\mu_i,\mu_j)$. It agrees with the original haze M phase function to within 1% for all values of cos Θ presented.

Once the $p_\ell(\mu_i,\mu_j)$ were obtained, the infinitesimal generators of the star semigroup were calculated (see Eq. (24) of I). Further details of the discrete ordinate method are given in I.

The stability of the doubling equations was tested by calculating the total flux for a conservative scattering atmosphere for various optical depths up to τ = 4,096. The flux was conserved in all instances to 1 part in 10^5. It is particularly noteworthy that the entire calculation which includes the computation of the reflected and transmitted radiance for optical depths up to 4,096, 21 angles of incidence, and Lambert ground albedos of 0, 0.2, and 1.0 took only 4 minutes on a CDC 7600.

3. Upward Radiance for Haze M Model

The results of calculations for the upward radiance of photons interacting with a haze M layer are presented in this section and compared with the results for Rayleigh scattering given in I. The incoming solar flux is normalized to unity in all cases. The upward radiance at the top of the haze layer is given in Figs. 2a, 2b, and 3a for μ_o (cosine of solar zenith angle) = 1, A (surface albedo) = 0, 0.2, and 1. When the optical depth is small and A = 0, the upward radiance is proportional to the single scattering function for the angle of scattering divided by μ, the cosine of the zenith angle; the radiance has a minimum for intermediate values of μ. As τ increases through the value 1, the maximum value of the radiance moves from the horizon to larger μ values, until for large values of τ the maximum is at the zenith with a horizon darkening. In all of the curves for upward radiance, the last plotted points for the largest τ value in each figure define the limiting curve for large τ; the points for larger τ values do not deviate from this limiting curve by more than the width of the symbols.

When A = 0.2 (Fig. 2b), the upward radiance is independent of μ for small τ. As τ increases, the radiance first decreases at the horizon and then increases. When A = 1 (Fig. 3a) the upward radiance at the horizon decreases as τ increases, while the value at the zenith increases.

The particular value μ_o = 0. 5379 was chosen in order to give an example of the radiance variations at another solar zenith angle. The upward radiance is given in Fig. 4 when A = 0 and ϕ = 0° and 180°. The azimuthal angle ϕ is measured from the incident plane which contains the incident ray and the zenith

direction; the antisolar point occurs when $\phi = 180°$. Thus as μ varies from the left to the right in Fig. 4, we obtain the radiance values from the solar horizon to the nadir and then back through the antisolar point to the antisolar horizon. The radiance for $\tau << 1$ increases much more near the solar horizon as μ approaches 0 than for Rayleigh scattering; it shows an increase at the antisolar point (corresponding to the increase in the phase function as the scattering angle approaches 180°).

The limiting curve for large τ is asymmetric with larger radiance values near the solar horizon. The corresponding radiance curves for $\phi = 90°$ are shown in Fig. 3b; for large τ there is horizon darkening in this plane which is at right angles to the incident plane.

As an example of the case when the sun is near the horizon, the value $\mu_o = 0.1882$ was chosen. The upward radiance is shown in Fig. 5 when $A = 0$ and $\phi = 0°$ and 180°. When $\tau << 1$, the radiance decreases almost four orders of magnitude from the solar horizon to the nadir and reaches a minimum value on the other side of the nadir ($\phi = 180°$); there is a slight increase in the radiance at the antisolar point.. The limiting curve for large τ is markedly asymmetric falling more than an order of magnitude from the solar horizon to the nadir while showing relatively little variation from the nadir to the antisolar horizon. There is much less variation with μ in the limiting curve for Rayleigh scattering (Fig. 5 of I).

The radiance varies much more with ϕ for haze M than for Rayleigh scattering. The radiance in the plane $\phi = 60°$ and 120° is shown in Fig. 6 and for $\phi = 90°$ in Fig. 7a. The radiance near the solar horizon for a given value of τ decreases more than an order of magnitude from the point with $\phi = 0°$ to $\phi = 90°$. In the curves of Figs. 6 and 7a, horizon brightening changes to

horizon darkening as τ increases. The limiting curve for large τ has a slight maximum above the solar horizon.

The next set of curves is for A = 0.2. The upward radiance for μ_o = 0.5379, A = 0.2, and ϕ = 90° is shown in Fig. 7b. When $\tau << 1$, the radiance is independent of μ since all of the photons have been reflected from the assumed Lambert surface. As τ increases a maximum develops in the radiance curve at an intermediate value of μ. The limiting curve for large values of τ is the same as that in Fig. 3b, since the surface albedo does not influence the reflected radiance when τ is sufficiently large.

The upward radiance when μ_o = 0.5379, A = 0.2, and ϕ = 0° and 180° is given in Fig. 8. As τ increases, the radiance becomes very asymmetric about the nadir. The same curves for ϕ = 60° and 120° are given in Fig. 9 to illustrate how these curves vary with ϕ. In this plane horizon darkening soon develops as τ increases.

The upward radiance for μ_o = 0.5379, A = 0.2, and ϕ = 0° and 180° is given in Fig. 9. The maximum radiance for a given value of τ is near the solar horizon when τ is small, but moves away from the horizon as τ increases. These curves are much less asymmetrical about the nadir than those in the plane with ϕ = 0° and 180°. The curves have to become completely symmetrical about the nadir in the plane with ϕ = 90°.

The upward radiance when μ_o = 0.1882, A = 0.2, and ϕ = 0° and 180° is shown in Fig. 10. The radiance has a pronounced maximum near the solar horizon in this plane. Even when τ = 0.001953 the radiance increases appreciably toward the solar horizon from its otherwise constant value. The radiance near the nadir decreases at first as τ increases from a very small initial value. At

first this behavior may seem paradoxical, but of course the radiance is increasing with τ at other angles so that the upward flux always increases with τ. Near the nadir there are very few single scattered photons from haze M, since the probability of single scattering through angles near 90° is very small (see Fig. 1). Thus, near the nadir the haze layer, as it becomes thicker, at first removes more photons scattered into this direction from the Lambert planetary surface (A = 0.2) than are added by scattering from the haze.

The radiance for the same parameters, but in the plane with $\phi = 90°$ is shown in Fig. 11a. The radiance still decreases at first with increasing τ near the nadir. The limiting curve for large τ shows relatively little variation with μ. These curves have quite a different functional dependence than those for Rayleigh scattering (Figs. 7 and 8a of I). The Rayleigh curves in the principal plane are nearly symmetric and the limiting curve for large values of τ in the plane with $\phi = 90°$ has a maximum at the last computed point near the solar horizon.

The next set of curves is for the case A = 1. The radiance when $\mu_o = 0.5379$ and $\phi = 90°$ is given in Fig. 11b. The radiance decreases at all angles as τ increases and approaches a limiting curve for large τ around $\tau = 4$. There is horizon darkening. The variation with μ of the radiance in the principal plane is qualitatively similar to that given in Fig. 12 and is not shown here.

The radiance when $\mu_o = 0.1882$, A = 1, and $\phi = 0°$ and 180° is given in Fig. 12 and for $\phi = 90°$ in Fig. 13a. The radiance develops a strong maximum near the solar horizon in the principal plane with a minimum near the nadir; there is little variation with μ from the nadir to the anti-solar horizon. This is quite different from the Rayleigh curve (Fig. 9 of I) which is

nearly symmetric about the nadir. The radiance for haze M shows an interesting variation as τ increases (Fig. 13a) with the limiting curve developing a maximum at an intermediate value of μ. Again this is very different from the Rayleigh curve (Fig. 8b).

4. Downward Radiance for Haze M Model

In this section the results are presented for the downward radiance at the bottom of the haze layer as calculated by the discrete ordinate method. The results are given for three values of the surface albedo, A = 0, 0.2, and 1. The downward radiance for these three values of the albedo is given in Figs. 13b, 14a, and 14b respectively for $\mu_o = 1$. When $\tau << 1$ the radiance has maxima at both the zenith and nadir with a minimum at an intermediate value of μ. The radiance increases some as A increases, the increase being greater at the horizon than at the zenith. The large value for the radiance at the zenith is due to the large probability of small angle scattering events with this phase function; there is no increase in the radiance at the zenith for Rayleigh scattering (Figs. 10a, 10b, 11a of I).

The maximum value of the diffuse flux (not including the direct beam) occurs for all values of A when $\tau \sim 1$. When $\tau >> 1$ the radiance depends critically on the value of A. When A = 0 the radiance curve approaches a limiting functional form with limb darkening, but shifts downward as τ increases. The curves are qualitatively the same when A = 0.2, but all radiance values are greater because of the photons reflected from the Lambert surface. When $\tau >> 1$ and A = 1, the downward radiance is a constant independent of μ; since there is no absorption the radiation becomes isotropic at great depths in this case.

The amount of limb darkening for large values of τ depends only on the nature of the medium, but not on the solar zenith angle, since the photon loses all memory of its initial direction through multiple collisions. Van de Hulst (1968) has given an asymptotic form for the transmitted radiance at the lower boundary of a medium and has shown that it is proportional to

$(\tau + C)^{-1}$, where C is a constant for a given medium. The radiance values for large τ obtained from our calculation vary as $(\tau + 7.874)^{-1}$ to a good approximation for any value of μ and μ_o. The ratio of the downward radiance at the zenith to the value near the horizon (last computed point $\mu = 0.03785$ or $\theta = 87.83°$) for large values of τ is 3.346, 2.416, and 1.000 when A = 0, 0.2, and 1 respectively. The same value to four significant figures is obtained for this ratio for any value of μ_o and for any value of τ such that $\tau \geq 64$. For Rayleigh scattering the corresponding values of the ratio are 2.713, 2.115, and 1.000 for A = 0, 0.2, and 1. Thus there is considerably more limb darkening under a thick cloud with haze M scattering than for one with Rayleigh scattering. It is possible to determine some of the scattering properties of the cloud layer even when it is very thick from a measurement of the horizon darkening.

The downward radiance for $\mu_o = 0.5379$, A = 0, and $\phi = 0°$ and 180° is shown in Fig. 15. When $\tau<1$, there is a strong peak in the diffuse radiance around the solar direction, which disappears for large value of τ. There is also a strong minimum in the radiance curve when $\tau<1$ in the plane with $\phi = 180°$. The curve for $\tau = 4$ is transitional, while the asymptotic form is closely approached for $\tau \geq 16$. For a given value of τ the downward radiance is greater for haze M than for Rayleigh scattering; more photons are sent downward in the haze M model because of the greater probability of small angle scattering. In the plane for $\phi = 60°$ and 120° (Fig 16) the radiance values are more nearly symmetric around the zenith than in Fig. 15. In the plane for $\phi = 90°$ (Fig. 17a) horizon brightening changes to horizon darkening around $\tau \sim 1$.

The downward radiance for $\mu_o = 0.1882$, A = 0, and $\phi = 0°$ and 180° is

given in Fig. 18. As τ increases the peak in the diffuse flux near the solar direction slowly moves toward the zenith. When $\tau \geq 16$, the limiting distribution has essentially been reached and the maximum radiance is at the zenith. It is interesting to compare these values with those for Rayleigh scattering (Fig. 13 of I). The haze M values for $\tau << 1$ are an order of magnitude greater near the solar horizon and an order of magnitude less near the zenith. In Fig. 17b the radiance is given in the plane for $\phi = 90°$; especially interesting is the change from limb brightening to limb darkening as τ increases as well as the change in the μ value for the maximum radiance on each curve. The maximum radiance near the zenith occurs when $\tau \sim 1$ for Rayleigh scattering (Fig. 11b of I), and for $\tau \sim 4$ for haze M scattering. In the latter case more optical depth is required to build up the diffuse radiance because of the smaller probability of scattering angles near 90°.

Two examples are given here when A = 0.2, both in the $\phi = 90°$ plane: $\mu_o = 0.5379$ (Fig. 19a) and $\mu_o = 0.1882$ (Fig. 19b). A moderate change in the surface albedo causes only small variations in the downward radiance. The largest change with surface albedo occurs near the horizon with much smaller changes near the zenith.

The downward radiance when $\mu_o = 0.5379$, A = 1, and $\phi = 0°$ and 180° is given in Fig. 20. The radiance values for $\tau << 1$ are greater than when A = 0 (Fig. 15), most noticeably from the zenith to the horizon when $\phi = 180°$. When $\tau \geq 16$ the downward radiance approaches a constant limiting value since no absorption has been assumed in the system. The radiance for $\phi = 90°$ is given in Fig. 21a. When $\tau < 1$ there is limb brightening.

The downward radiance is shown in Fig. 22 for $\mu_o = 0.1882$, A = 1,

and $\phi = 0°$ and 180°. The curves for small values of τ have qualitatively the same form as those for A = 0 (Fig. 18), but approach a constant value independent of μ, when $\tau >> 1$. It is instructive to compare these results for haze M scattering with those for Rayleigh scattering (Fig. 17 of I). The haze M values compared to the Rayleigh values for $\tau < 1$ are an order of magnitude larger near the solar horizon with a peak in the solar direction, are an order of magnitude smaller near the zenith, and are considerably smaller from the zenith to the antisolar horizon.

The downward radiance for $\mu_o = 0.1882$, A = 1, $\phi = 60°$ and 120° is given in Fig. 23 and for $\phi = 90°$ in Fig. 21b. When $\tau < 1$ there is horizon brightening. For Rayleigh scattering in the plane with $\phi = 90°$ the radiance at the horizon increases with increasing τ, reaches a maximum for $\tau \sim 0.1$, and then decreases to the limiting value for large τ. This effect is not nearly as marked for haze M scattering, because of the strong forward scattering and relatively small number of single scattering collisions that are made at angles near 90°.

5. Flux

The diffuse flux at the lower boundary for A = 0 is presented in Table I for three values of the solar zenith angle and for various optical thicknesses of the scattering layer. The values for Rayleigh and haze M scattering are given in the third and fourth columns respectively. The diffuse flux at the lower boundary is always greater for haze M than for Rayleigh scattering, since more photons are sent deep into the scattering medium by the numerous small angle scattering events with haze M compared to Rayleigh scattering.

The cloud albedo defined as the upward flux leaving the scattering layer per unit incident flux when A = 0 is given in columns five and six of Table I for Rayleigh and haze M scattering respectively. The single scattering function is considerably larger in the backward direction for Rayleigh compared to haze M scattering; thus the cloud albedo is always larger for a layer of given optical thickness scattering according to the Rayleigh than for haze M phase function.

The present exact results can be used to evaluate the accuracy of the Monte Carlo method. Kattawar and Plass (1968) have reported the flux for Rayleigh and haze M scattering for $\mu_o = 1$ and $\tau = 1$. The Monte Carlo results for the diffuse flux at the lower boundary for Rayleigh and haze M scattering with the discrete ordinate results in parenthesis are 0.289 (0.292) and 0.569 (0.569) respectively. The corresponding results for the cloud albedo are 0.343 (0.3405) and 0.0628 (0.0628). This comparison agrees with our previous statements that the Monte Carlo flux values are accurate within 1 to 2% except in unusual circumstances. Unfortunately this is the only case where the μ_o and τ values are the same in the two calculations.

6. Conclusions

The radiance and flux for both the reflected and transmitted photons has been calculated for a haze M layer by the discrete ordinate method over a range of optical thicknesses from very thin to very thick. The results are presented for three solar zenith angles and for three values of the surface albedo. A comparison of these results with the corresponding results for Rayleigh scattering shows a number of interesting features. The variation of the radiance with both μ and ϕ is more marked for scattering from a haze M than from a Rayleigh layer. The horizon darkening relative to the radiance at the zenith is greater for very thick haze M than for Rayleigh layers. The downward diffuse flux at the lower boundary for A = 0 is always greater for haze M than for Rayleigh layers of the same optical thickness, whereas the cloud albedo is always less for haze M.

This work was supported by Grant No. NGR 44-001-117 from the National Aeronautics and Space Administration.

Table I. Diffuse Flux and Cloud Albedo for A = 0

μ_o	τ	Diffuse flux at lower boundary		Cloud albedo	
		Rayleigh	Haze M	Rayleigh	Haze M
1	0.001953	9.759×10^{-4}	1.844×10^{-3}	9.753×10^{-4}	1.077×10^{-4}
	0.01562	7.754×10^{-3}	1.464×10^{-2}	7.750×10^{-3}	8.646×10^{-4}
	0.25	1.096×10^{-1}	2.067×10^{-1}	1.116×10^{-1}	1.448×10^{-2}
	1	2.917×10^{-1}	5.693×10^{-1}	3.405×10^{-1}	6.284×10^{-2}
	4	2.919×10^{-1}	7.212×10^{-1}	6.898×10^{-1}	2.604×10^{-1}
	16	9.677×10^{-2}	3.604×10^{-1}	9.032×10^{-1}	6.396×10^{-1}
	64	2.577×10^{-2}	1.166×10^{-1}	9.742×10^{-1}	8.834×10^{-1}
	256	6.550×10^{-3}	3.146×10^{-2}	9.935×10^{-1}	9.686×10^{-1}
	1024	1.644×10^{-3}	8.025×10^{-3}	9.984×10^{-1}	9.920×10^{-1}
	4096	4.115×10^{-4}	2.018×10^{-3}	9.996×10^{-1}	9.980×10^{-1}
0.5379	0.001953	1.812×10^{-3}	3.237×10^{-3}	1.812×10^{-3}	3.876×10^{-4}
	0.01562	1.431×10^{-2}	2.551×10^{-2}	1.432×10^{-2}	3.122×10^{-3}
	0.25	1.823×10^{-1}	3.202×10^{-1}	1.894×10^{-1}	5.163×10^{-2}
	1	3.612×10^{-1}	6.552×10^{-1}	4.830×10^{-1}	1.891×10^{-1}
	4	2.207×10^{-2}	5.388×10^{-1}	7.788×10^{-1}	4.607×10^{-1}
	16	6.881×10^{-2}	3.105×10^{-1}	9.313×10^{-1}	7.459×10^{-1}
	64	1.833×10^{-2}	8.223×10^{-2}	9.817×10^{-1}	9.177×10^{-1}
	256	4.657×10^{-3}	2.218×10^{-2}	9.954×10^{-1}	9.778×10^{-1}
	1024	1.169×10^{-3}	5.659×10^{-3}	9.988×10^{-1}	9.943×10^{-1}
	4096	2.926×10^{-4}	1.423×10^{-3}	9.997×10^{-1}	9.986×10^{-1}
0.1882	0.001953	5.164×10^{-3}	7.594×10^{-3}	5.164×10^{-3}	2.734×10^{-3}
	0.01562	3.983×10^{-2}	5.825×10^{-2}	3.986×10^{-2}	2.147×10^{-2}
	0.25	3.474×10^{-1}	4.891×10^{-1}	3.878×10^{-1}	2.462×10^{-1}
	1	3.394×10^{-1}	5.246×10^{-1}	6.558×10^{-1}	4.706×10^{-1}
	4	1.498×10^{-1}	3.427×10^{-1}	8.503×10^{-1}	6.574×10^{-1}
	16	4.661×10^{-2}	1.617×10^{-1}	9.534×10^{-1}	8.386×10^{-1}
	64	1.241×10^{-2}	5.232×10^{-2}	9.874×10^{-1}	9.476×10^{-1}
	256	3.155×10^{-3}	1.412×10^{-2}	9.970×10^{-1}	9.858×10^{-1}
	1024	7.918×10^{-4}	3.601×10^{-3}	9.991×10^{-1}	9.965×10^{-1}
	4096	1.982×10^{-4}	9.056×10^{-4}	9.997×10^{-1}	9.991×10^{-1}

REFERENCES

1. Dave, J. V. and J. Gazdag, 1970: A modified fourier transform method for multiple scattering calculations in a plane parallel Mie atmosphere. Appl. Opt. 9, 1457-1466.
2. Deirmendjian, D., 1969: Electromagnetic Scattering on Spherical Polydispersions. New York, American Elsevier Publishing Co., Inc., 290 pp.
3. Grant, I. P. and G. E. Hunt, 1969: Discrete space theory of radiative transfer. Proc. Roy. Soc. Long. A313, 183-216.
4. Hansen, J. E., 1969: Exact and approximate solutions for multiple scattering by cloudy and hazy planetary atmospheres. J. Atmos. Sci. 26, 478-487.
5. Kattawar, G. W. and G. N. Plass, 1967: Electromagnetic scattering from absorbing spheres. Appl. Opt., 6, 1377-1382.
6. Kattawar, G. W. and G. N. Plass, 1968: Influence of particle size distribution on reflected and transmitted light from clouds. Appl. Opt. 7, 869-878.
7. Plass, G. N., G. W. Kattawar, and F. E. Catchings, 1972: Discrete ordinate theory of radiative transfer: I. Rayleigh scattering. J. Atmos. Sci. (in press).
8. Preisendorfer, R. W., 1965: Radiative Transfer on Discrete Spaces. New York, Pergamon Press, 459 pp.
9. Twomey, S., H. Jacobowitz, and H. B. Howell, 1966: Matrix methods for multiple-scattering problems. J. Atmos. Sci., 23, 289-296.
10. Van de Hulst, 1968: Asymptotic fitting, a method for solving anisotropic transfer problems in thick layers. J. Computational Phys. 3, 291-306.

Legend for Figures

Fig. 1. Single scattering phase function for haze M as a function of the cosine of the scattering angle μ. The upper right inset shows the phase function for scattering angles near 180°.

Fig. 2. Upward radiance at top of the atmosphere for haze M scattering for $\mu_o = 1$ as a function of the cosine of the nadir angle μ. Each curve is for a particular value of the optical thickness τ (see legend on Fig. 3). The left hand figure is for A = 0 (Fig. 2a) and the right hand figure is for A = 0.2 (Fig. 2b). The limiting curve for large τ is the same as the last plotted curve within the width of the symbols. All curves are normalized to unit incident flux.

Fig. 3a. Upward radiance for $\mu_o = 1$ and A = 1; Fig. 3b. $\mu_o = 0.5379$, A = 0, and $\phi = 90°$. See legend to Fig. 2.

Fig. 4. Upward radiance for $\mu_o = 0.5379$, A = 0, and $\phi = 0°$ and 180°. See legend to Fig. 2.

Fig. 5. Upward radiance for $\mu_o = 0.1883$, A = 0, and $\phi = 0°$ and 180°. See legend to Fig. 2.

Fig. 6. Upward radiance for $\mu_o = 0.1882$, A = 0, and $\phi = 60°$ and 120°. See legend to Fig. 2.

Fig. 7a. Upward radiance for $\mu_o = 0.1882$, A = 0, and $\phi = 90°$; Fig. 7b. $\mu_o = 0.5379$, A = 0.2, and $\phi = 90°$. See legend to Fig. 2.

Fig. 8. Upward radiance for $\mu_o = 0.5379$, A = 0.2, and $\phi = 0°$ and 180°. See legend to Fig. 2.

Fig. 9. Upward radiance for $\mu_o = 0.5379$, A = 0.2, and $\phi = 60°$ and 120°. See legend to Fig. 2.

Fig. 10. Upward radiance for $\mu_o = 0.1882$, $A = 0.2$, and $\phi = 0°$ and 180°. See legend to Fig. 2.

Fig. 11a. Upward radiance for $\mu_o = 0.1882$, $A = 0.2$, and $\phi = 90°$; Fig. 22b. $\mu_o = 0.5379$, $A = 1$, $\phi = 90°$. See legend to Fig. 2.

Fig. 12. Upward radiance for $\mu_o = 0.1882$, $A = 1$, and $\phi = 0°$ and 180°. See legend to Fig. 2.

Fig. 13a. Upward radiance for $\mu_o = 0.1882$, $A = 1$, and $\phi = 90°$; Fig. 13b. downward radiance for $\mu_o = 1$ and $A = 0$. See legend to Fig. 2.

Fig. 14a. Downward radiance for $\mu_o = 1$ and $A = 0.2$; Fig. 14b. $\mu_o = 1$ and $A = 1$. See legend to Fig. 2.

Fig. 15. Downward radiance for $\mu_o = 0.5379$, $A = 0$, and $\phi = 0°$ and 180°. See legend to Fig. 2.

Fig. 16. Downward radiance for $\mu_o = 0.5379$, $A = 0$, and $\phi = 60°$ and 120°. See legend to Fig.2.

Fig. 17a. Downward radiance for $\mu_o = 0.5379$, $A = 0$, and $\phi = 90°$; Fig. 17b. $\mu_o = 0.1882$, $A = 0$, and $\phi = 90°$. See legend to Fig. 2.

Fig. 18. Downward radiance for $\mu_o = 0.1882$, $A = 0$, and $\phi = 0°$ and 180°. See legend to Fig. 2.

Fig. 19a. Downward radiance for $\mu_o = 0.5379$, $A = 0.2$, and $\phi = 90°$; Fig. 19b. $\mu_o = 0.1882$, $A = 0.2$, and $\phi = 90°$. See legend to Fig. 2.

Fig. 20. Downward radiance for $\mu_o = 0.5379$, $A = 1$, and $\phi = 0°$ and 180°. See legend to Fig. 2.

Fig. 21a. Downward radiance for $\mu_o = 0.5379$, $A = 1$, $\phi = 90°$; Fig. 21b. $\mu_o = 0.1882$, $A = 1$, $\phi = 90°$. See legend to Fig. 2.

Fig. 22. Downward radiance for $\mu_o = 0.1882$, $A = 1$, $\phi = 0°$ and 180°. See legend to Fig. 2.

Fig. 23 Downward radiance for $\mu_o = 0.1882$, $A = 1$, and $\phi = 60°$ and 120°. See legend to Fig. 2.

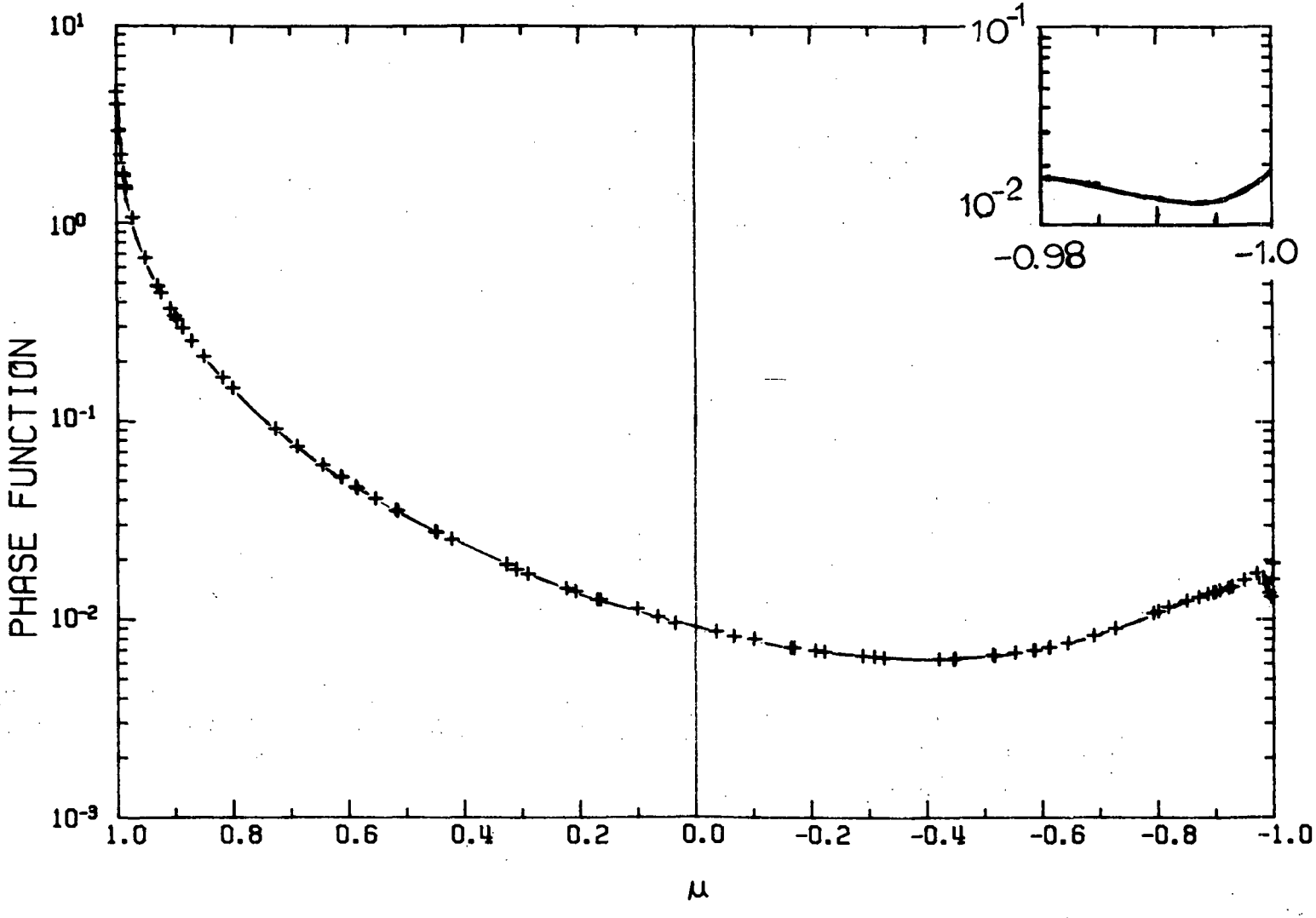
PHASE FUNCTION
10^{1}
10^{0}
10^{-1}
10^{-2}
10^{-3}
1.0
0.8
0.6
0.4
0.2
0.0
-0.2
-0.4
-0.6
-0.8
-1.0
μ
10^{-1}
10^{-2}
-0.98
-1.0

Fig. 1

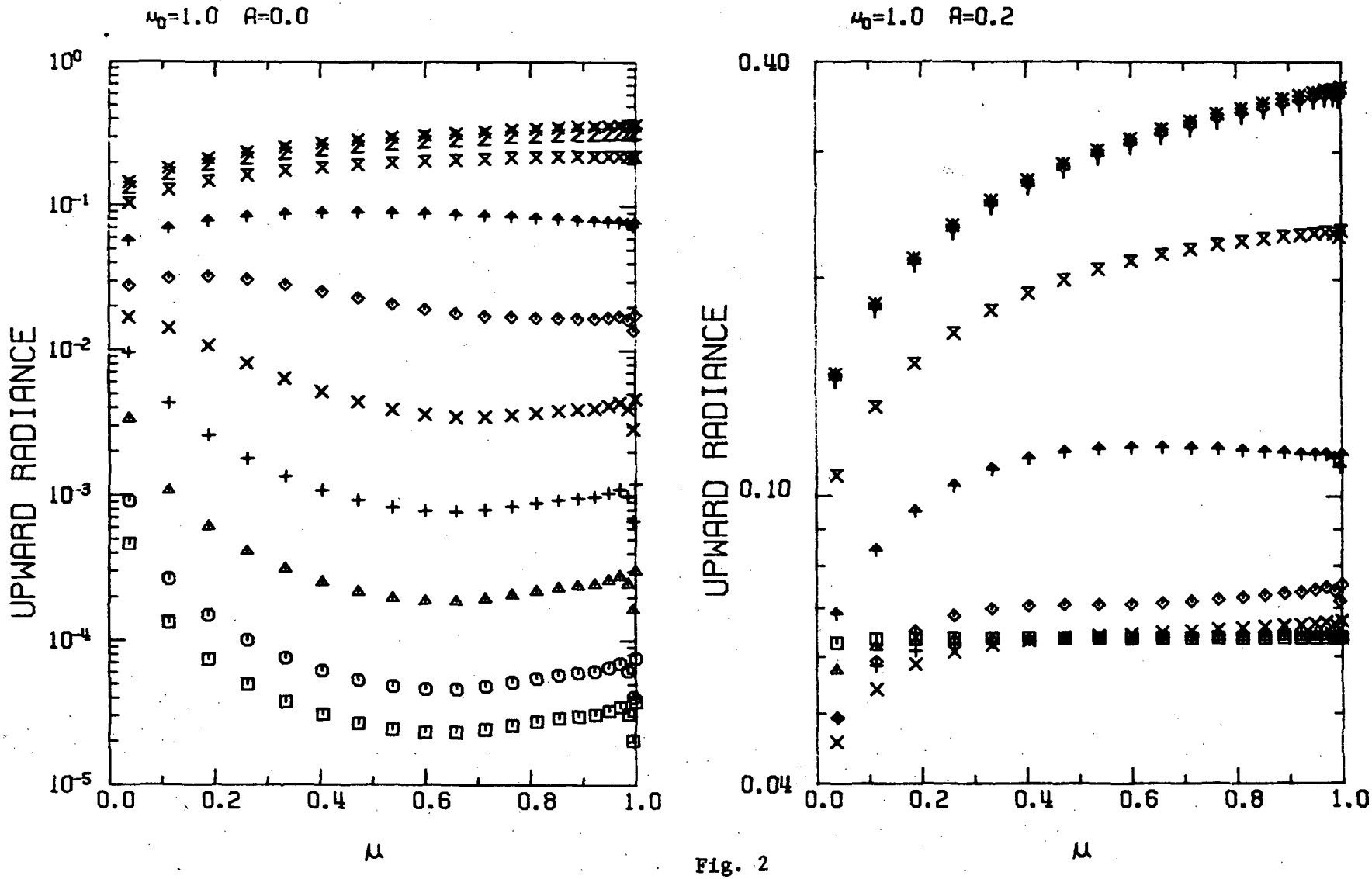
μ_0=1.0 A=0.0
UPWARD RADIANCE
10^0
10^{-1}
10^{-2}
10^{-3}
10^{-4}
10^{-5}
0.0
0.2
0.4
0.6
0.8
1.0
μ
μ_0=1.0 A=0.2
UPWARD RADIANCE
0.40
0.10
0.04
0.0
0.2
0.4
0.6
0.8
1.0
μ

Fig. 2

a.

b.

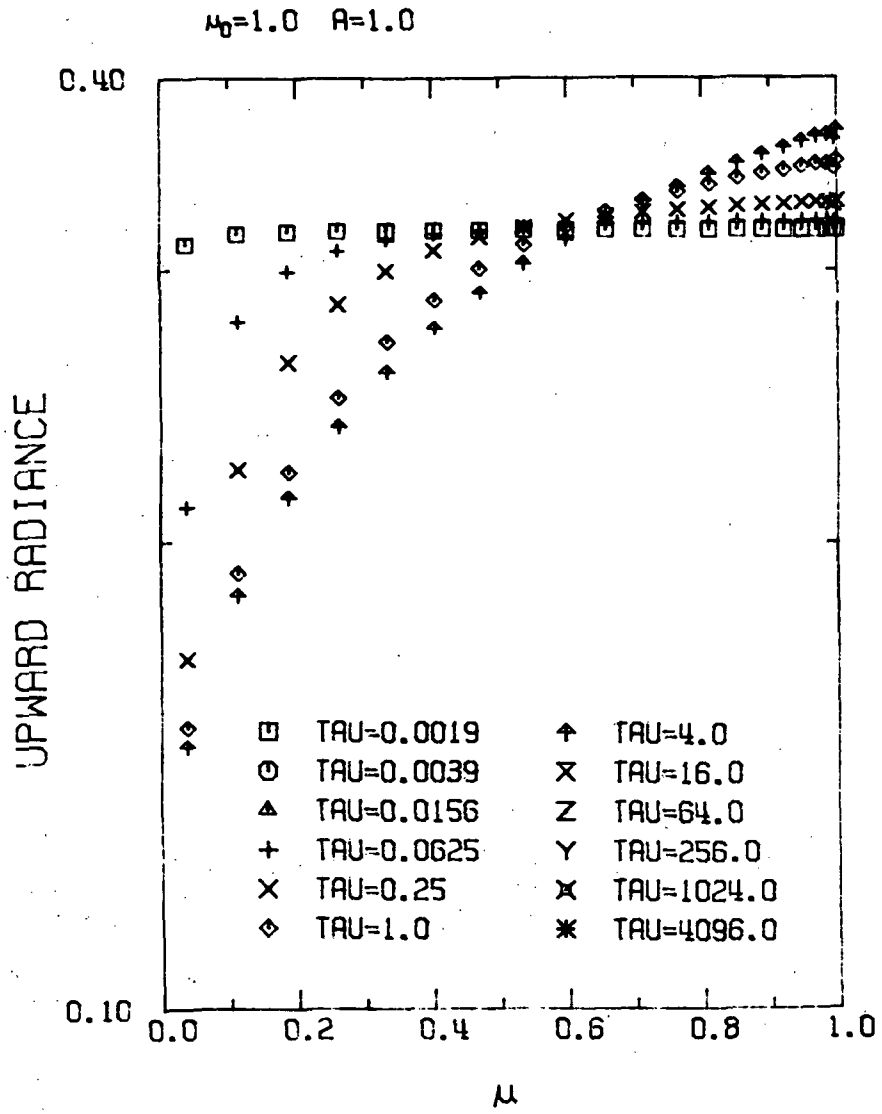
μ_0=1.0 A=1.0
0.40
0.10
UPWARD RADIANCE
0.0
0.2
0.4
0.6
0.8
1.0
μ
TAU=0.0019
TAU=0.0039
TAU=0.0156
TAU=0.0625
TAU=0.25
TAU=1.0
TAU=4.0
TAU=16.0
TAU=64.0
TAU=256.0
TAU=1024.0
TAU=4096.0

a.

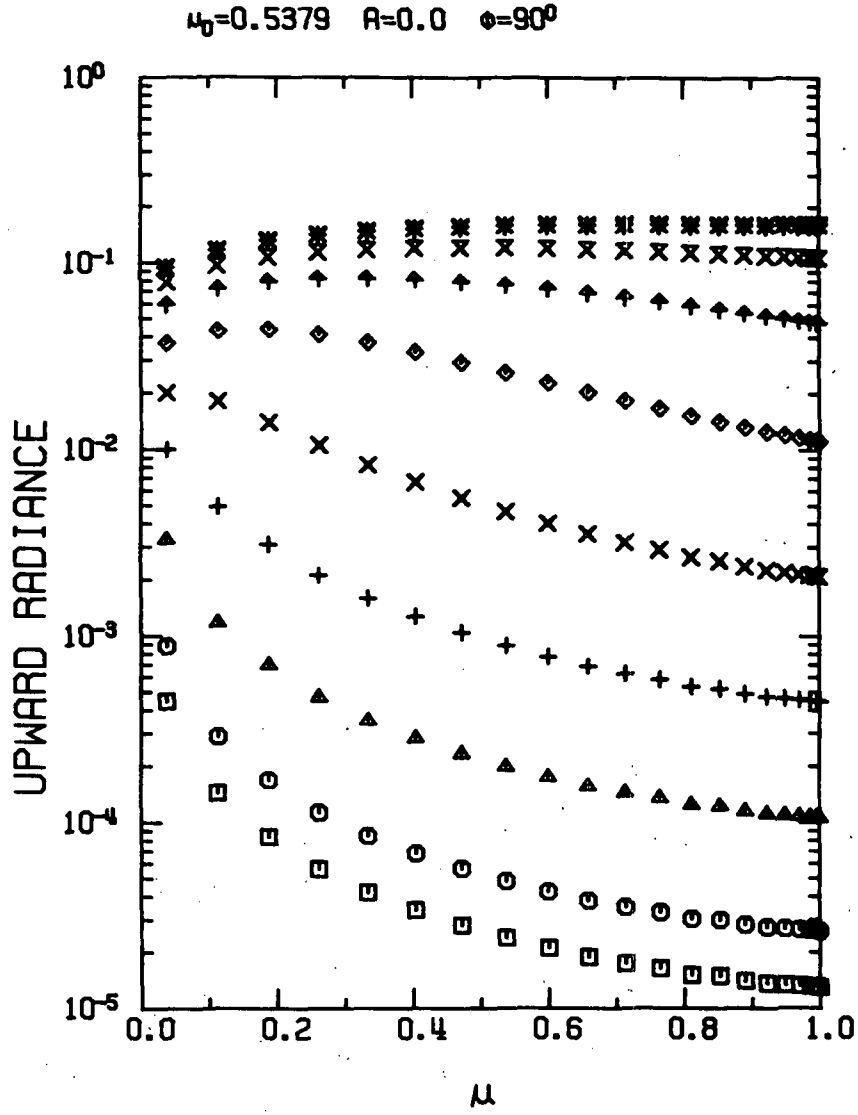
μ_0=0.5379 A=0.0 ϕ=90°
10^0
10^{-1}
10^{-2}
10^{-3}
10^{-4}
10^{-5}
UPWARD RADIANCE
0.0
0.2
0.4
0.6
0.8
1.0
μ

b.

Fig. 3

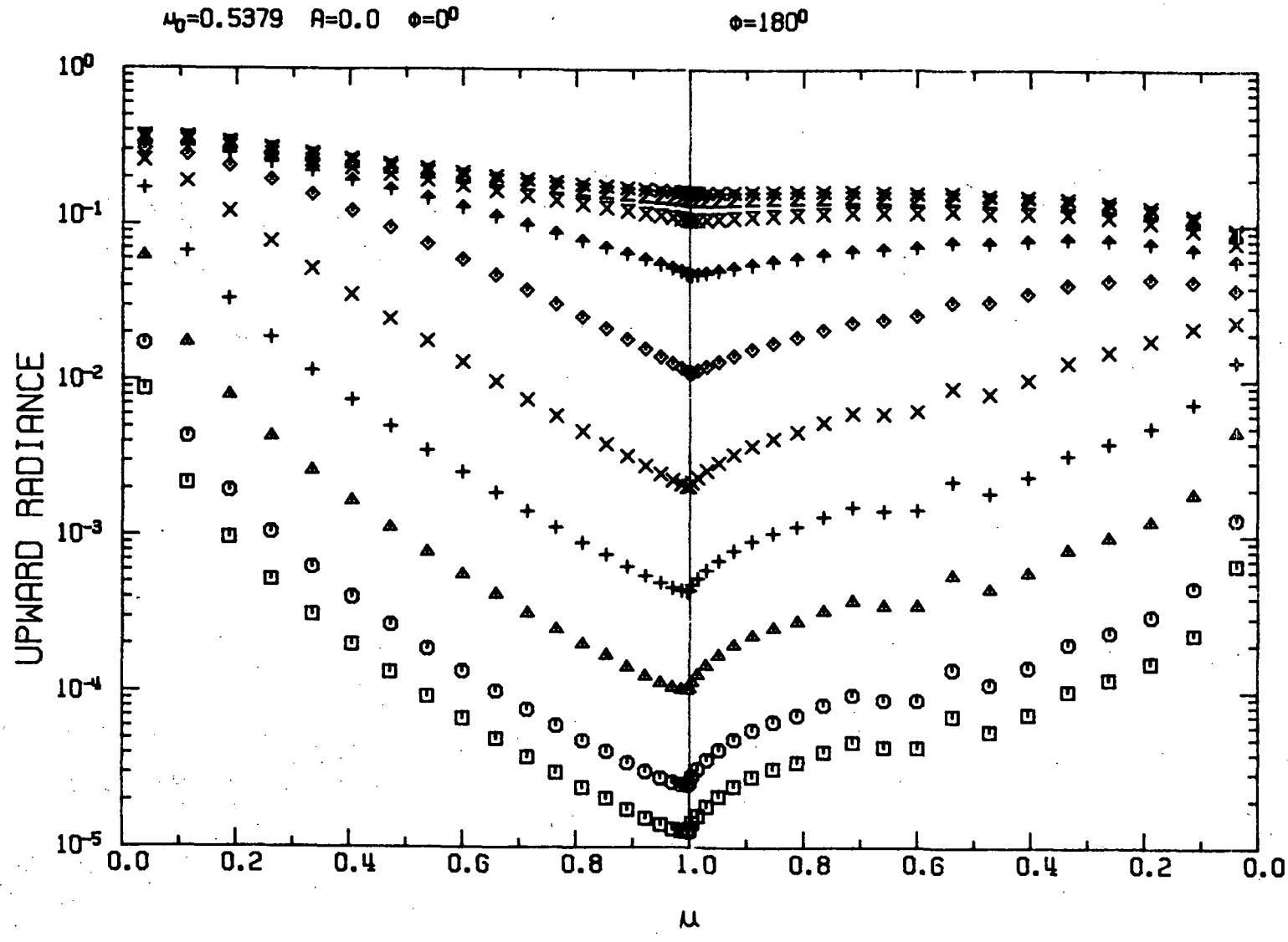
μ_0=0.5379 A=0.0 ϕ=0^0
ϕ=180^0
UPWARD RADIANCE
10^0
10^{-1}
10^{-2}
10^{-3}
10^{-4}
10^{-5}
0.0
0.2
0.4
0.6
0.8
1.0
0.8
0.6
0.4
0.2
0.0
μ

Fig. 4

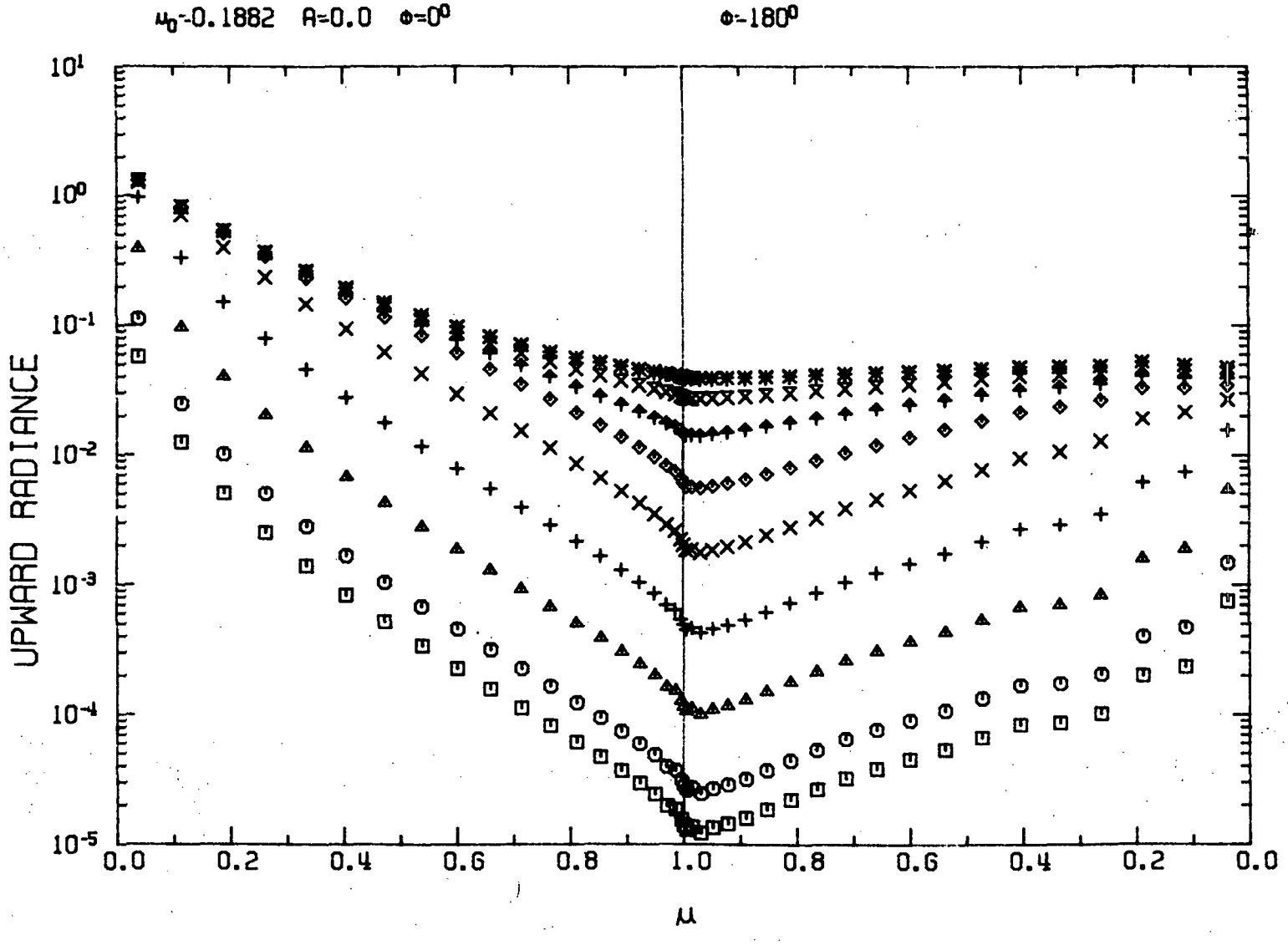
μ_0=0.1882 A=0.0 ϕ=0°
ϕ=180°
UPWARD RADIANCE
10^{1}
10^{0}
10^{-1}
10^{-2}
10^{-3}
10^{-4}
10^{-5}
0.0 0.2 0.4 0.6 0.8 1.0 0.8 0.6 0.4 0.2 0.0
μ

Fig. 5

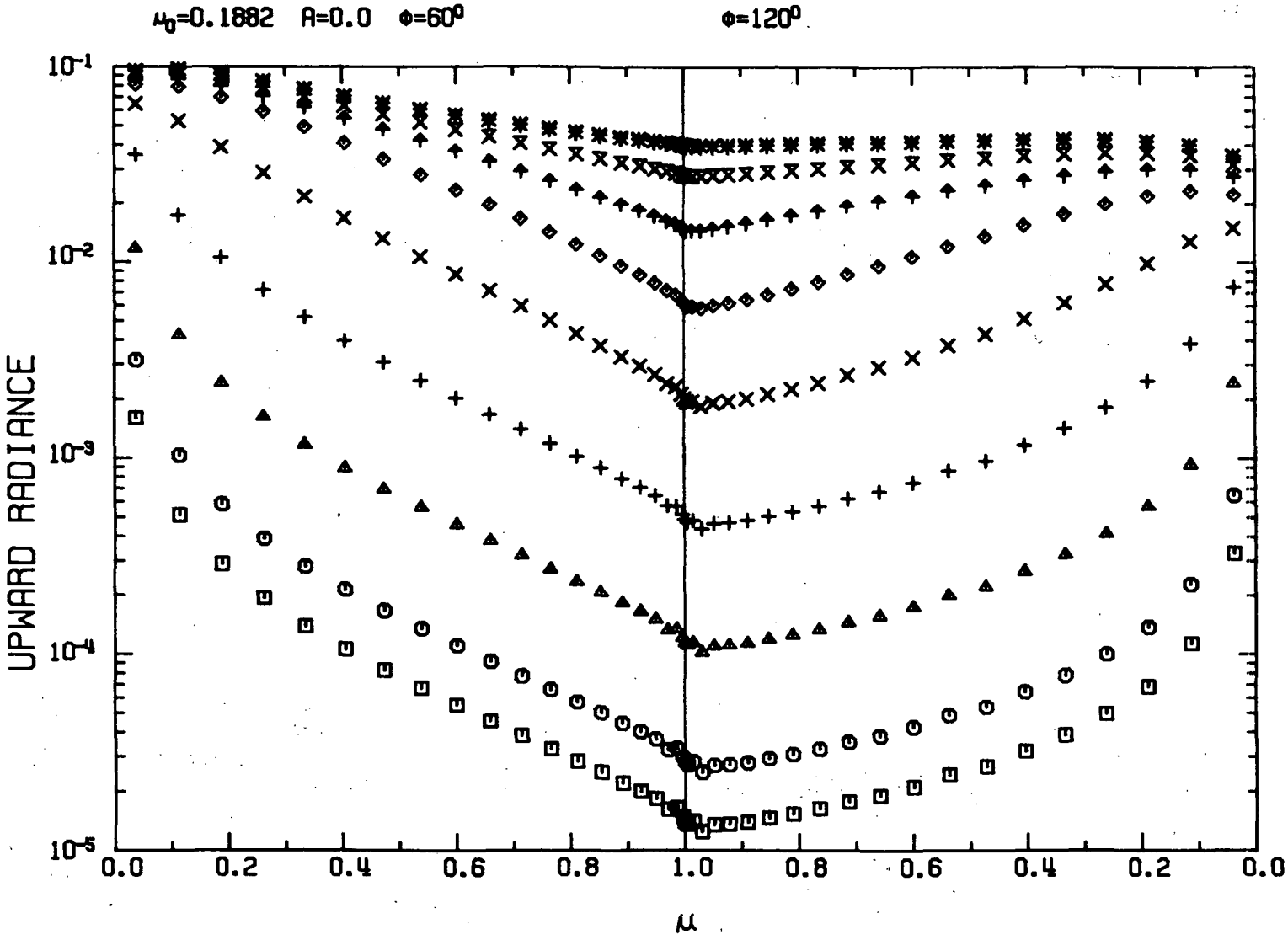
μ_0=0.1882 A=0.0 ϕ=60^0
ϕ=120^0
UPWARD RADIANCE
10^{-1}
10^{-2}
10^{-3}
10^{-4}
10^{-5}
0.0
0.2
0.4
0.6
0.8
1.0
0.8
0.6
0.4
0.2
0.0
μ

Fig. 6

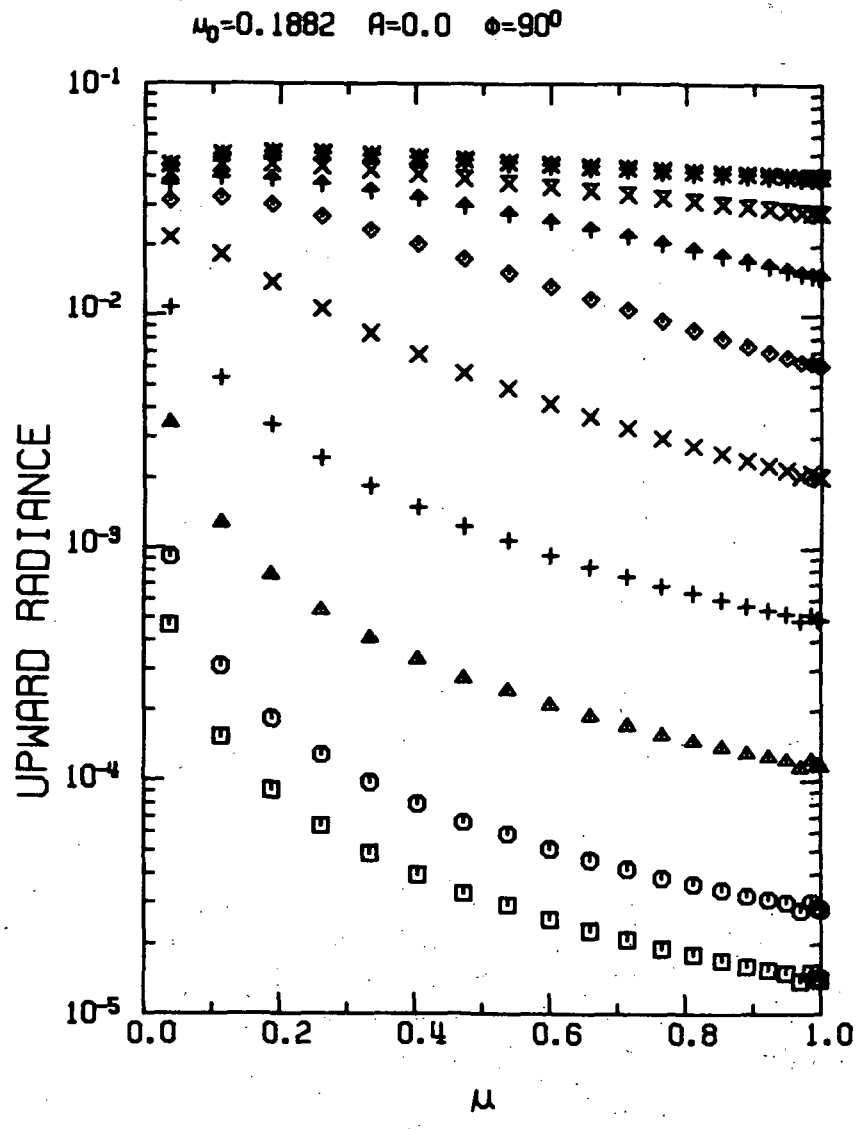
μ_0=0.1882 A=0.0 ϕ=90^0
UPWARD RADIANCE
10^{-1}
10^{-2}
10^{-3}
10^{-4}
10^{-5}
0.0
0.2
0.4
0.6
0.8
1.0
μ

a.

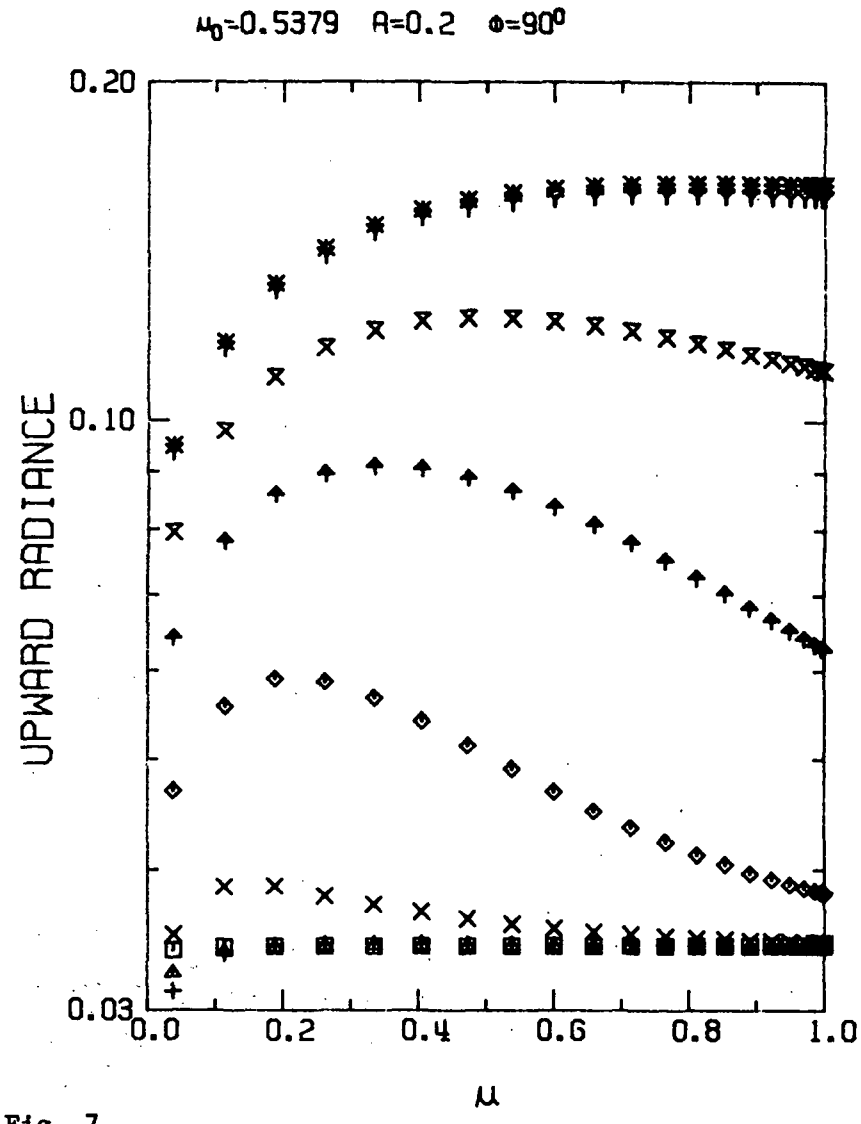
μ_0=0.5379 A=0.2 ϕ=90^0
UPWARD RADIANCE
0.20
0.10
0.03
0.0
0.2
0.4
0.6
0.8
1.0
μ

b.

Fig. 7

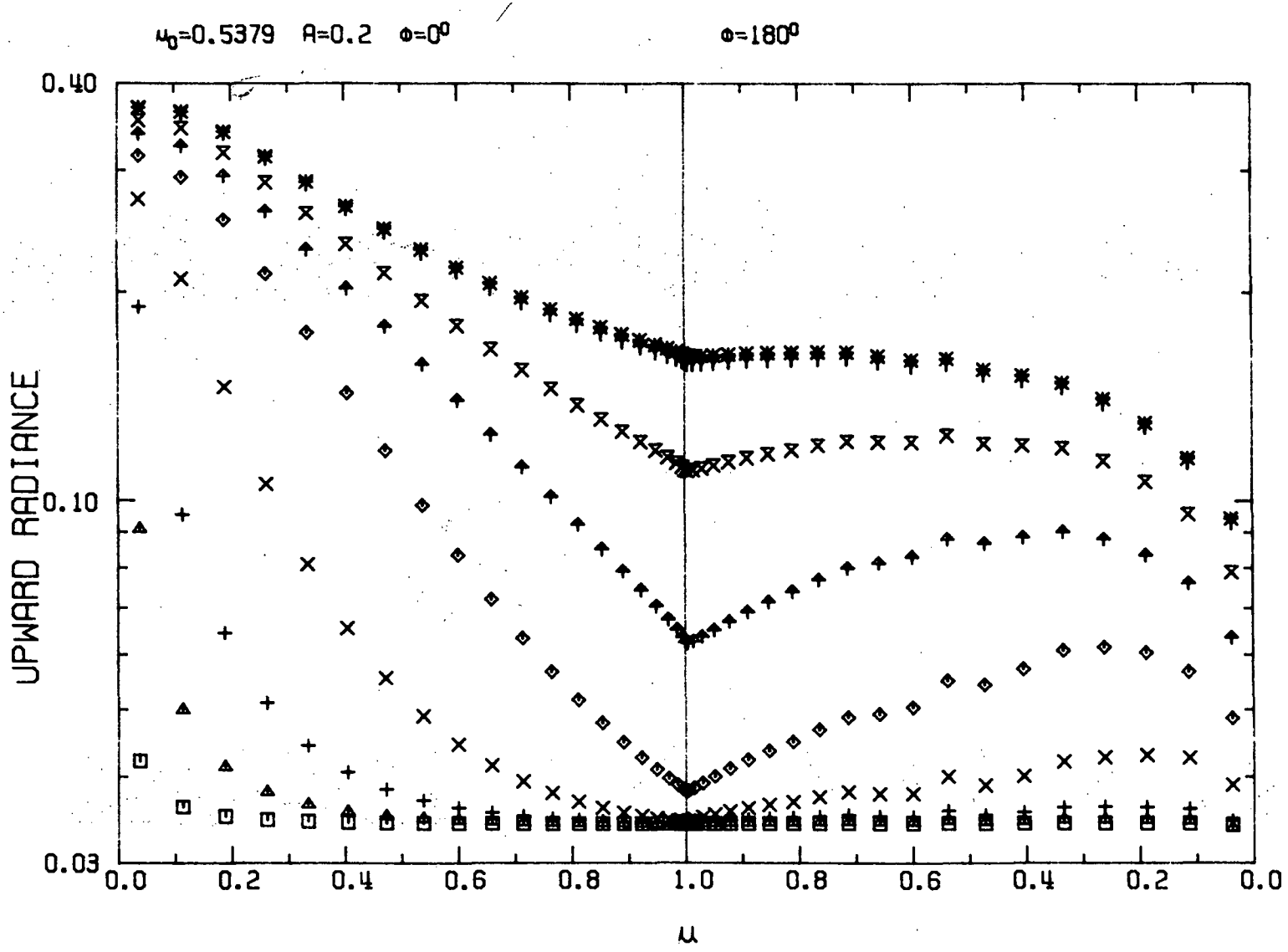
μ_0=0.5379 A=0.2 Φ=0^0
Φ=180^0
0.40
0.10
0.03
UPWARD RADIANCE
0.0
0.2
0.4
0.6
0.8
1.0
0.8
0.6
0.4
0.2
0.0
μ

Fig. 8

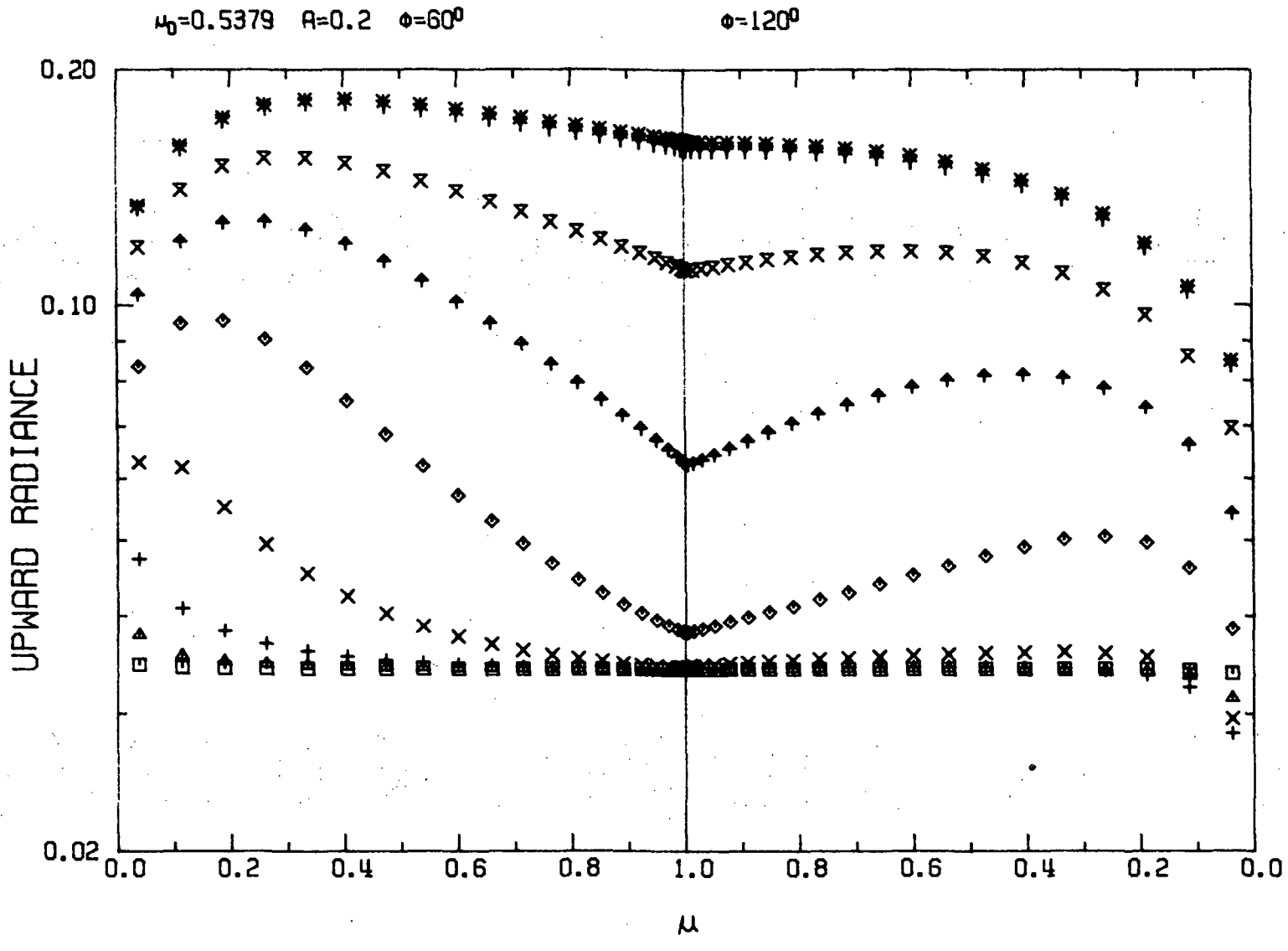
μ_0=0.5379 A=0.2 Φ=60^0
Φ=120^0
0.20
0.10
0.02
UPWARD RADIANCE
0.0
0.2
0.4
0.6
0.8
1.0
0.8
0.6
0.4
0.2
0.0
μ

Fig. 9

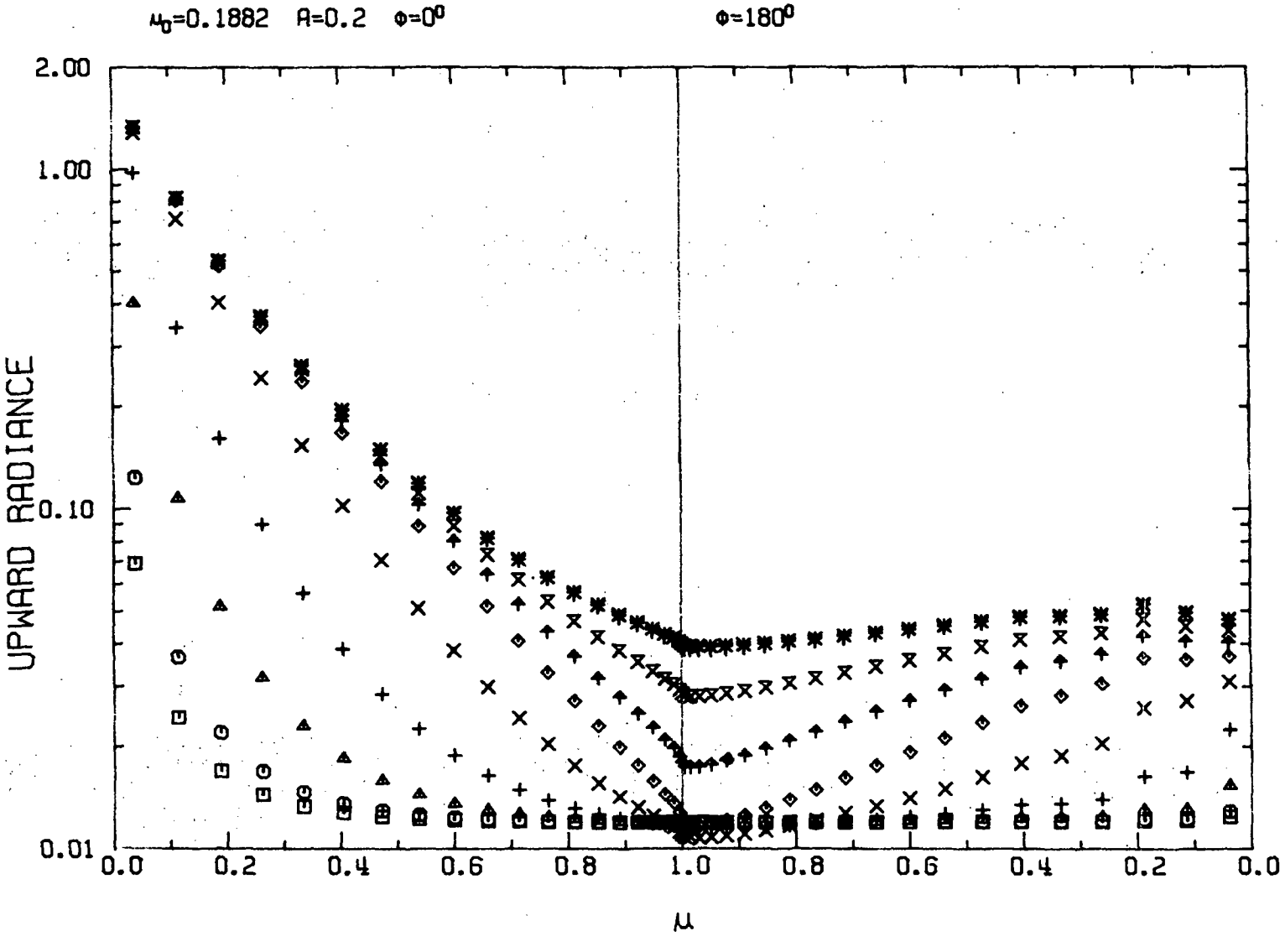
μ_0=0.1882 A=0.2 ϕ=0^0
ϕ=180^0
2.00
1.00
0.10
0.01
UPWARD RADIANCE
0.0
0.2
0.4
0.6
0.8
1.0
0.8
0.6
0.4
0.2
0.0
μ

Fig. 10

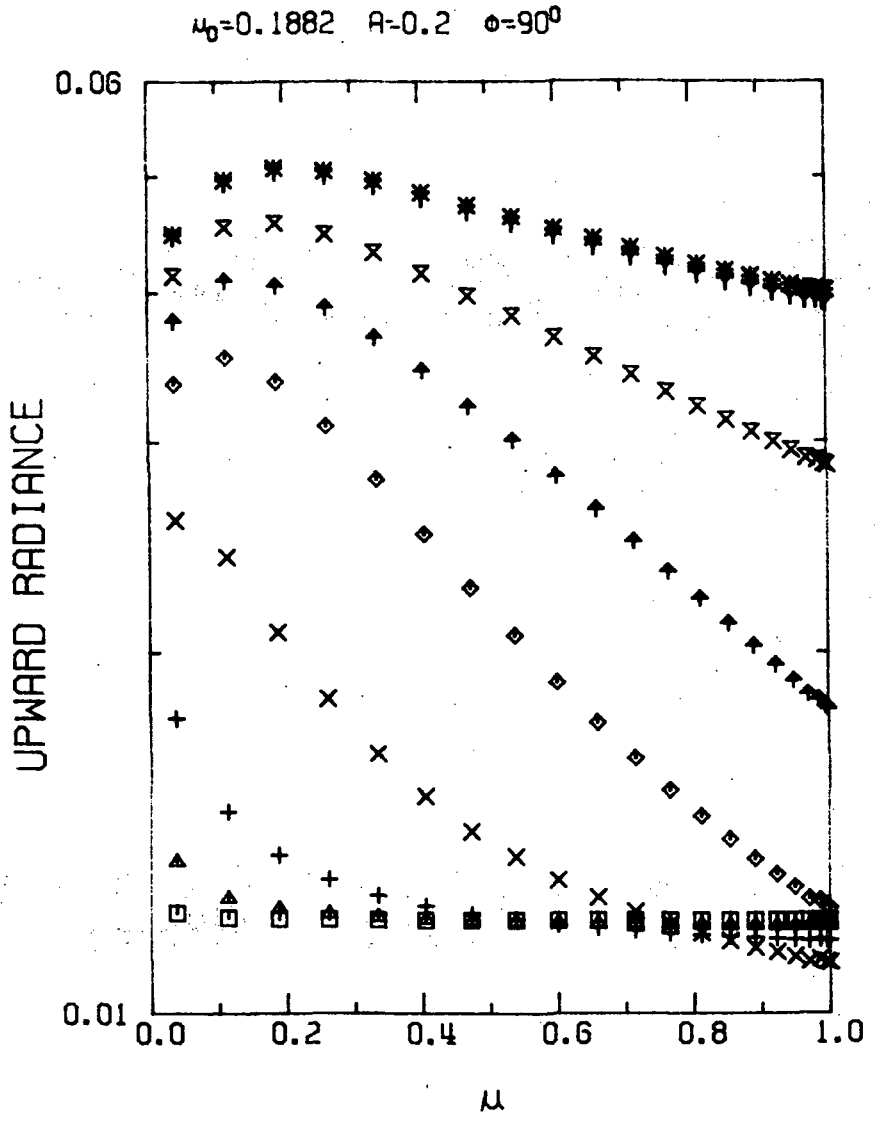
μ_0=0.1882 A=0.2 ϕ=90^0
0.06
0.01
UPWARD RADIANCE
0.0
0.2
0.4
0.6
0.8
1.0
μ

a.

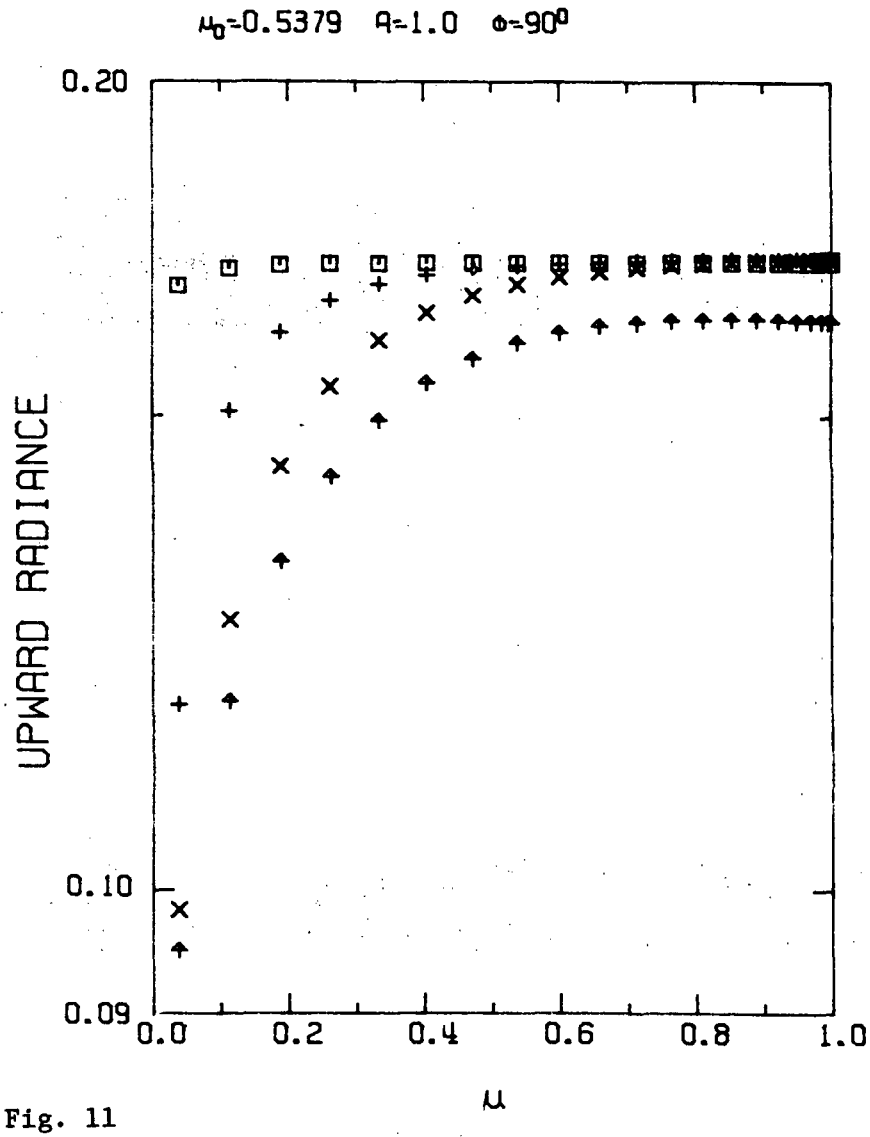
μ_0=0.5379 A=1.0 ϕ=90^0
0.20
0.10
0.09
UPWARD RADIANCE
0.0
0.2
0.4
0.6
0.8
1.0
μ

b.

Fig. 11

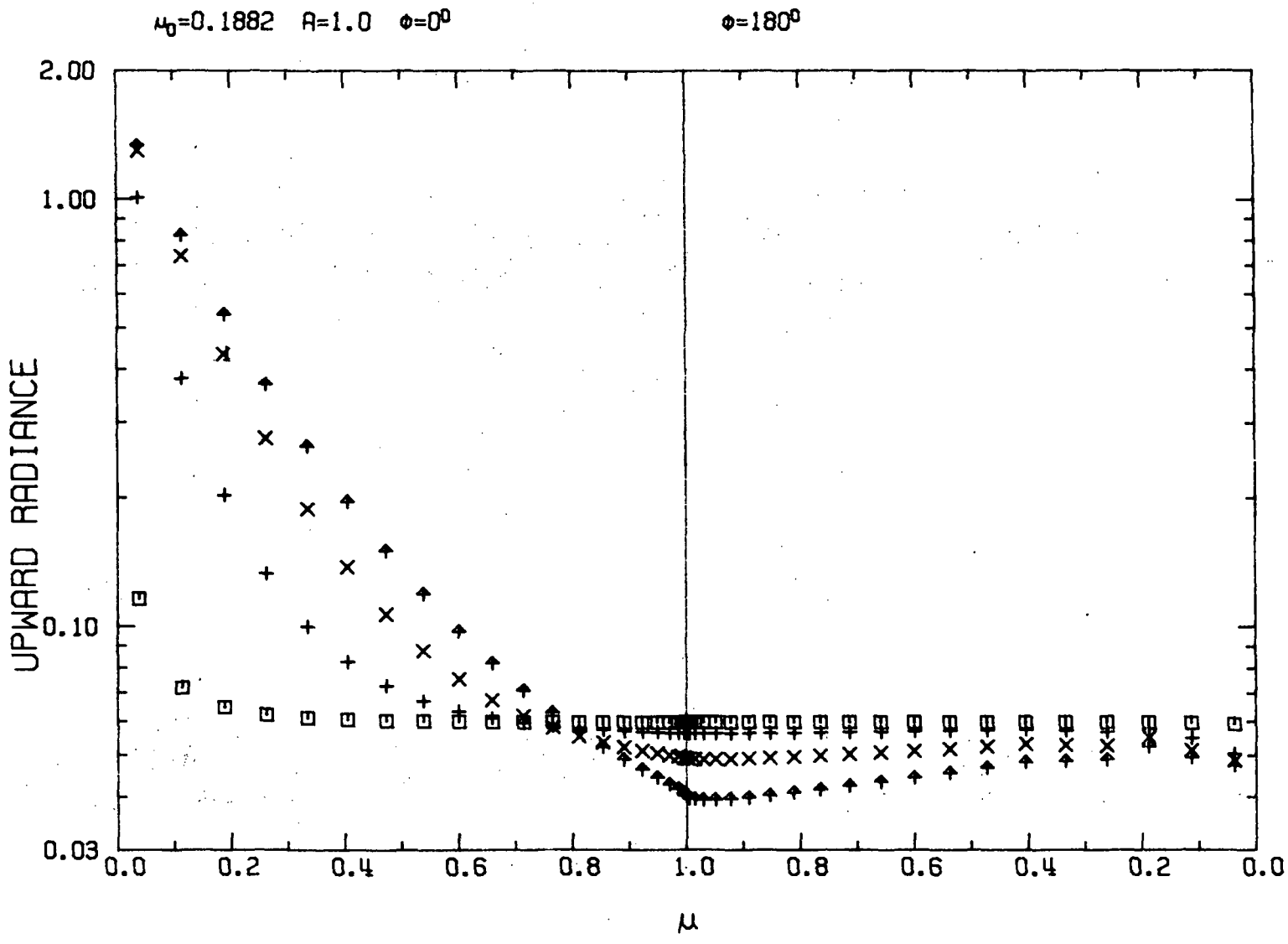
μ_0=0.1882 A=1.0 ϕ=0^0
ϕ=180^0
2.00
1.00
0.10
0.03
UPWARD RADIANCE
0.0
0.2
0.4
0.6
0.8
1.0
0.8
0.6
0.4
0.2
0.0
μ

Fig. 12

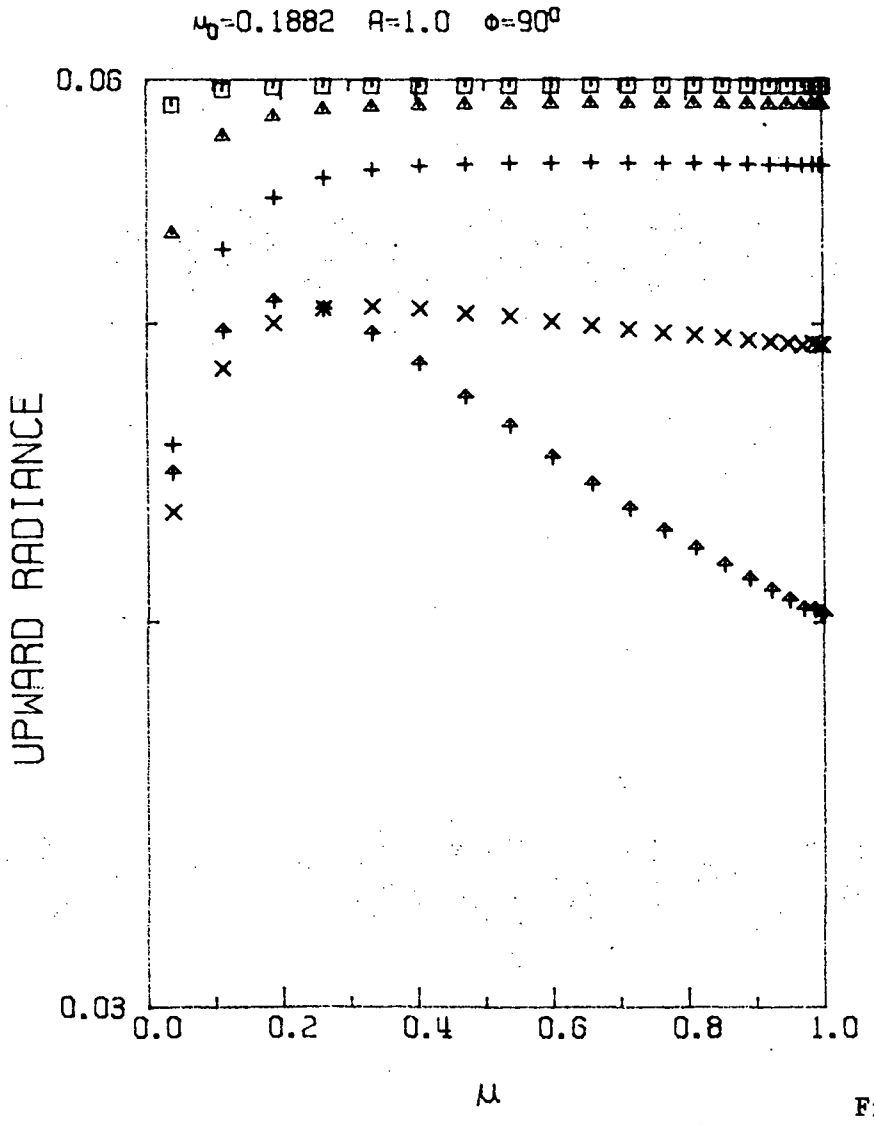
μ_0=0.1882 A=1.0 Φ=90°
0.06
0.03
UPWARD RADIANCE
0.0
0.2
0.4
0.6
0.8
1.0
μ

a.

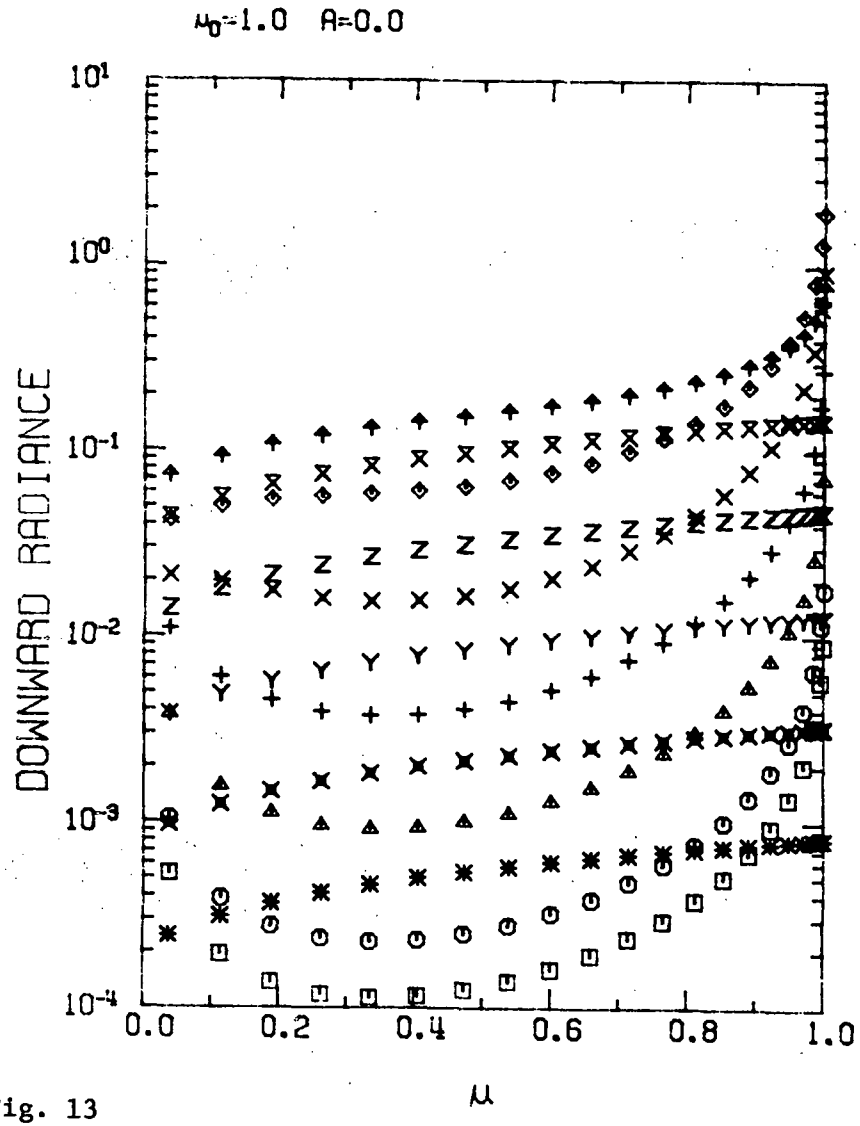
μ_0=1.0 A=0.0
10^{1}
10^{0}
10^{-1}
10^{-2}
10^{-3}
10^{-4}
DOWNWARD RADIANCE
0.0
0.2
0.4
0.6
0.8
1.0
μ

b.

Fig. 13

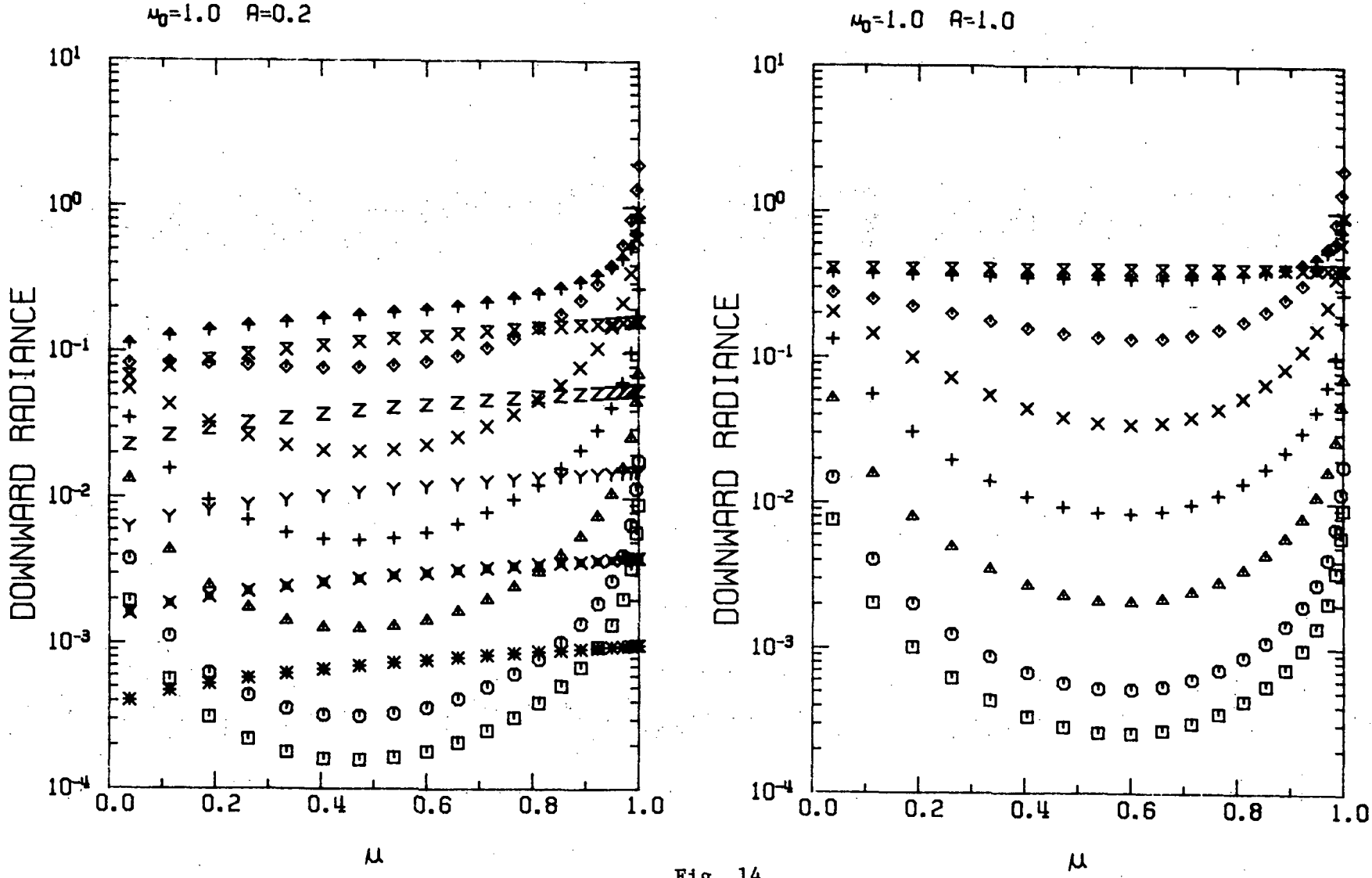
μ_0=1.0 A=0.2
DOWNWARD RADIANCE
10^1
10^0
10^{-1}
10^{-2}
10^{-3}
10^{-4}
0.0
0.2
0.4
0.6
0.8
1.0
μ
μ_0=1.0 A=1.0
DOWNWARD RADIANCE
10^1
10^0
10^{-1}
10^{-2}
10^{-3}
10^{-4}
0.0
0.2
0.4
0.6
0.8
1.0
μ

Fig. 14.

a.

b.

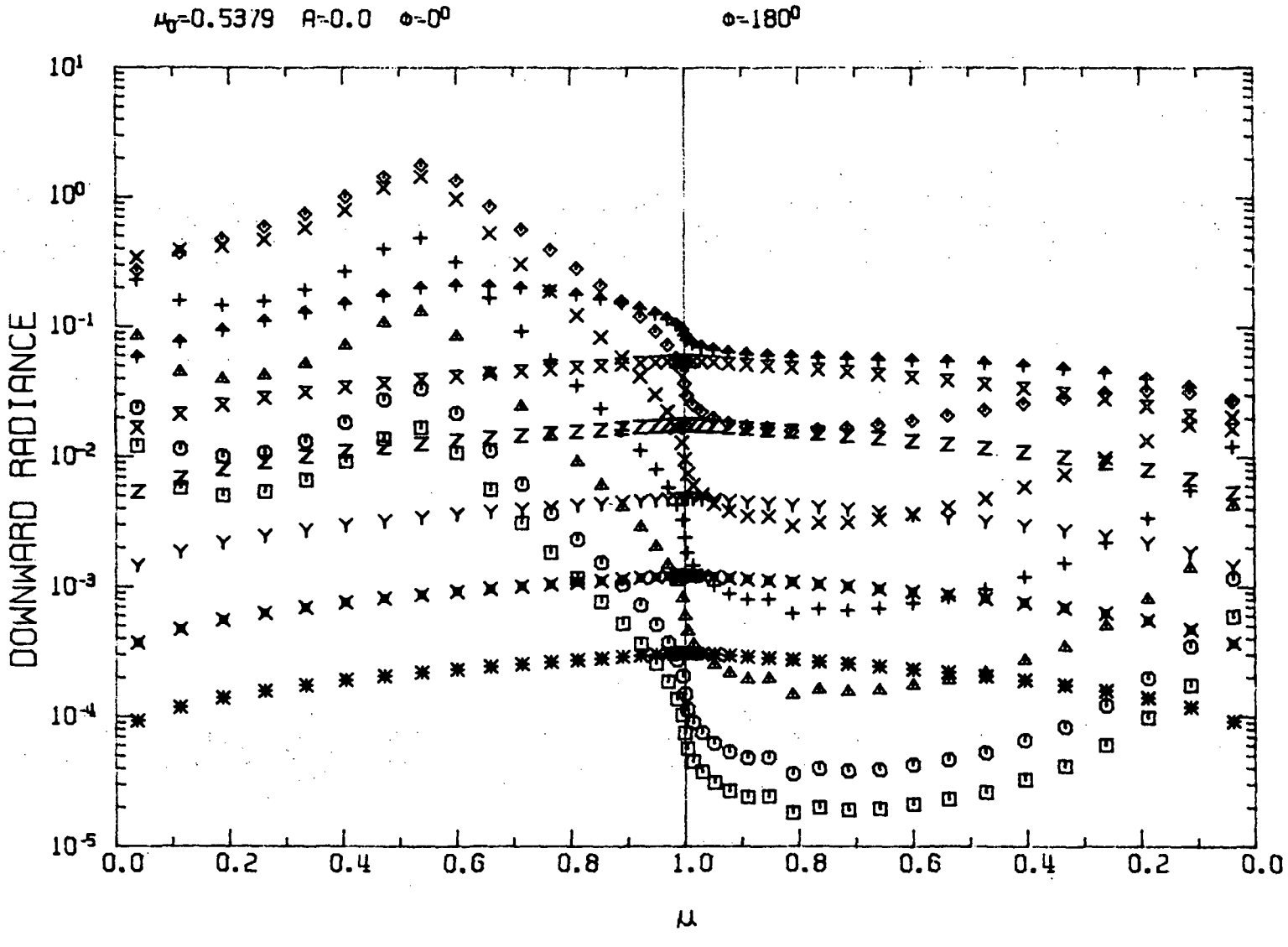
μ_0=0.5379 A=0.0 ϕ=0^0
ϕ=180^0
DOWNWARD RADIANCE
10^1
10^0
10^{-1}
10^{-2}
10^{-3}
10^{-4}
10^{-5}
0.0
0.2
0.4
0.6
0.8
1.0
0.8
0.6
0.4
0.2
0.0
μ

Fig. 15

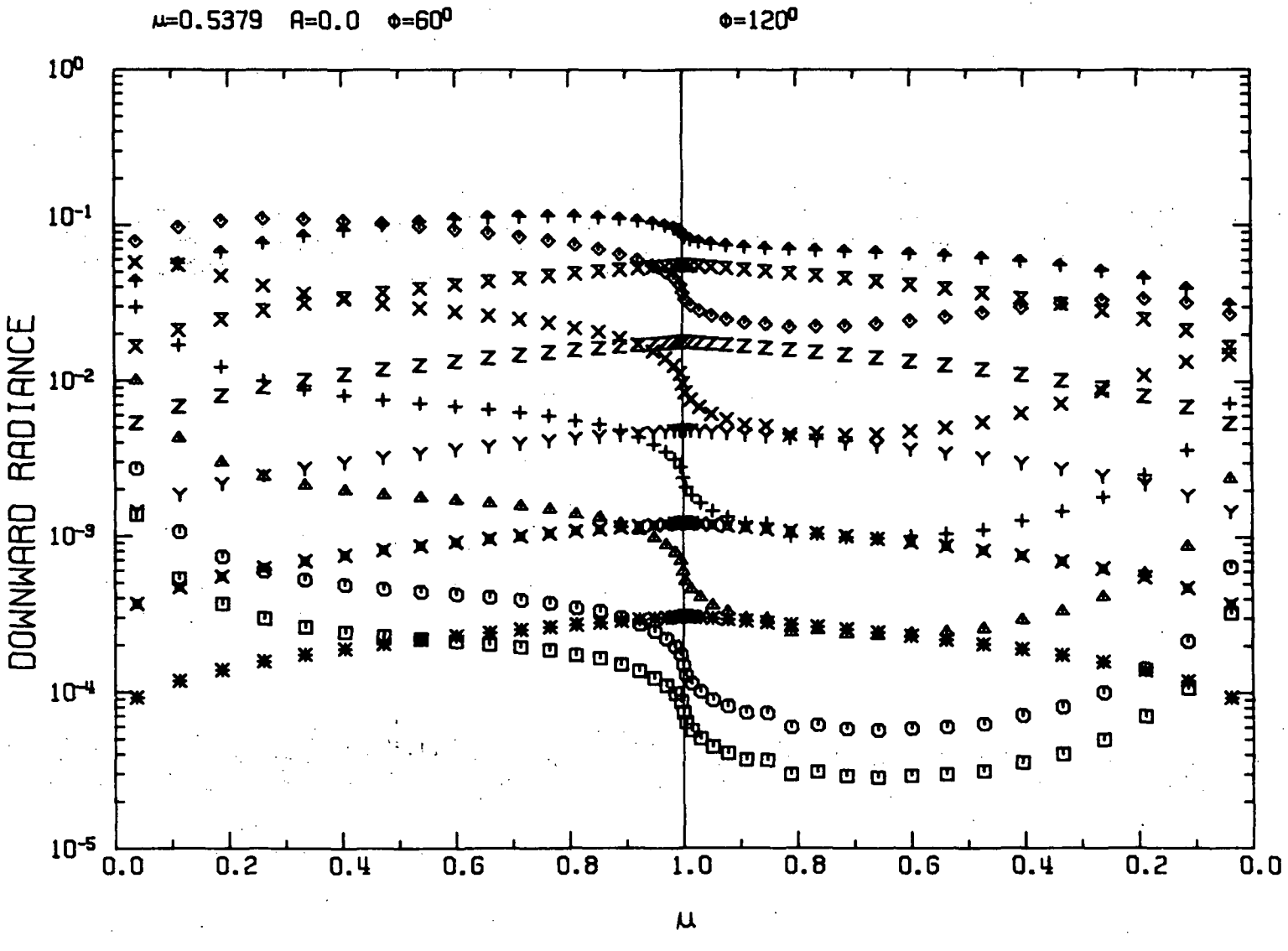
μ=0.5379 A=0.0 Φ=60⁰
Φ=120⁰
DOWNWARD RADIANCE
10⁰
10⁻¹
10⁻²
10⁻³
10⁻⁴
10⁻⁵
0.0
0.2
0.4
0.6
0.8
1.0
0.8
0.6
0.4
0.2
0.0
μ

Fig. 16

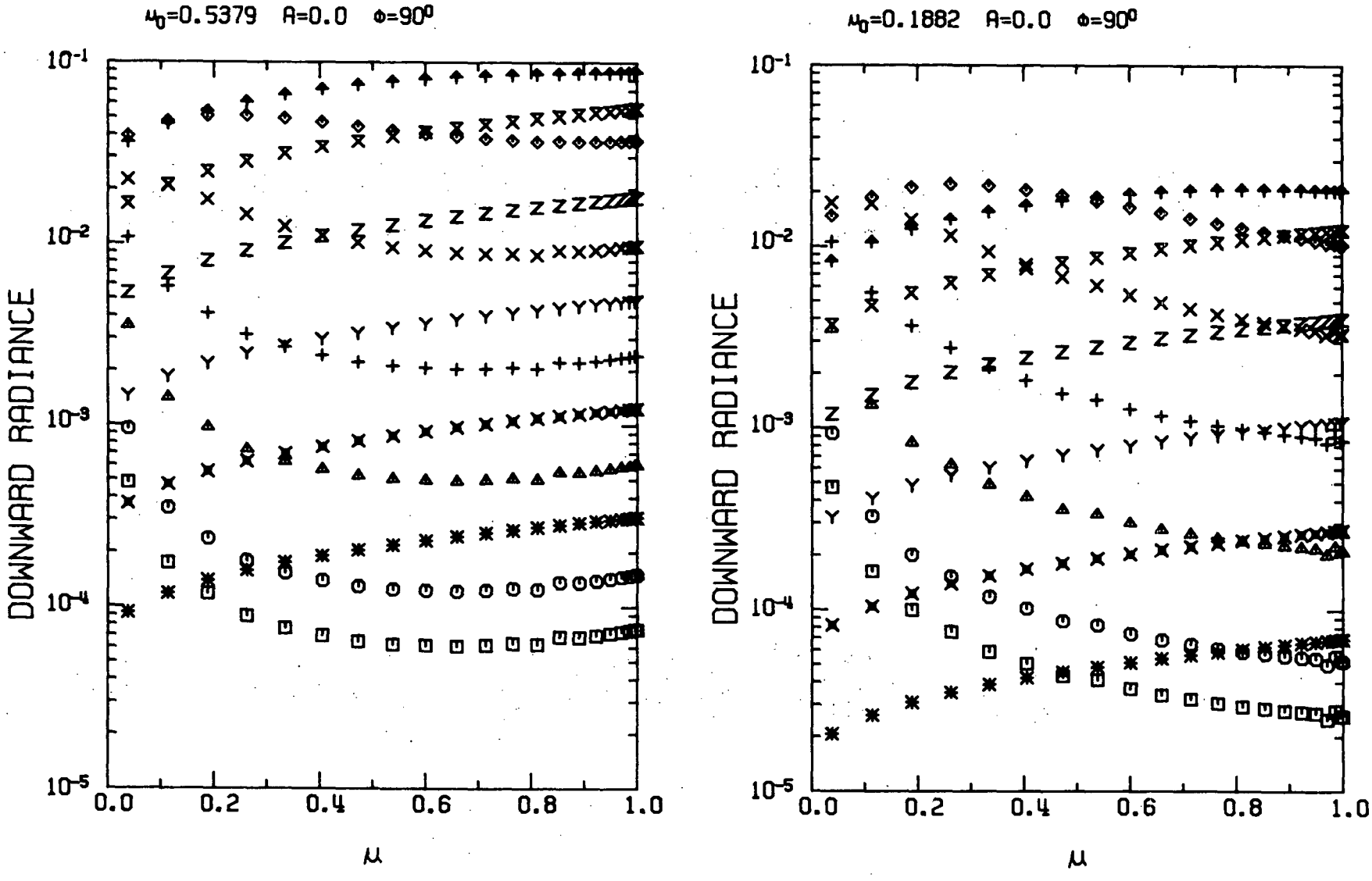
μ_0=0.5379 A=0.0 ϕ=90^0
μ_0=0.1882 A=0.0 ϕ=90^0
DOWNWARD RADIANCE
10^{-1}
10^{-2}
10^{-3}
10^{-4}
10^{-5}
0.0
0.2
0.4
0.6
0.8
1.0
μ

Fig. 17

a.

b.

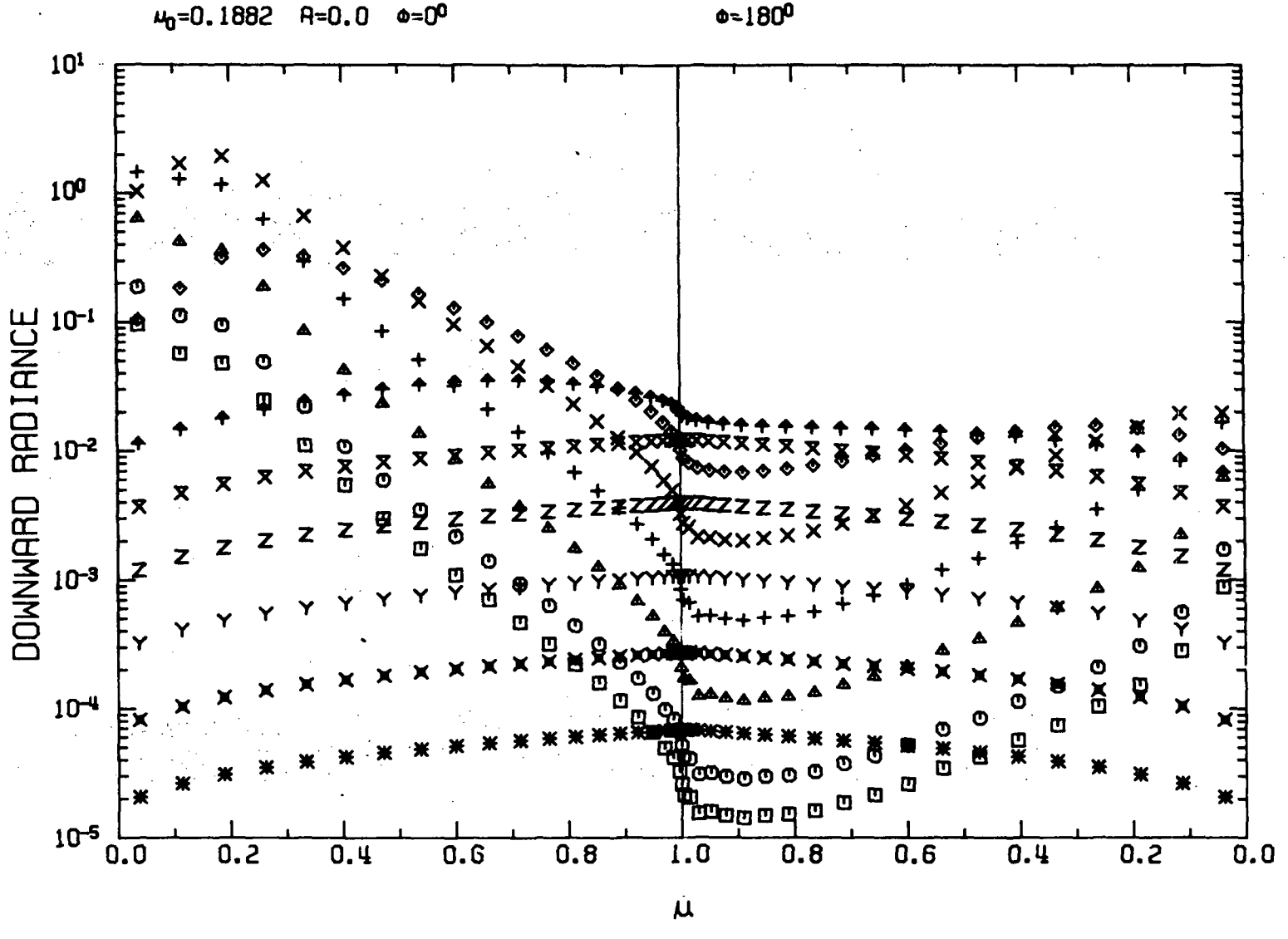
μ_0=0.1882 A=0.0 ϕ=0^0
ϕ=180^0
DOWNWARD RADIANCE
10^1
10^0
10^{-1}
10^{-2}
10^{-3}
10^{-4}
10^{-5}
0.0
0.2
0.4
0.6
0.8
1.0
0.8
0.6
0.4
0.2
0.0
μ

Fig. 18

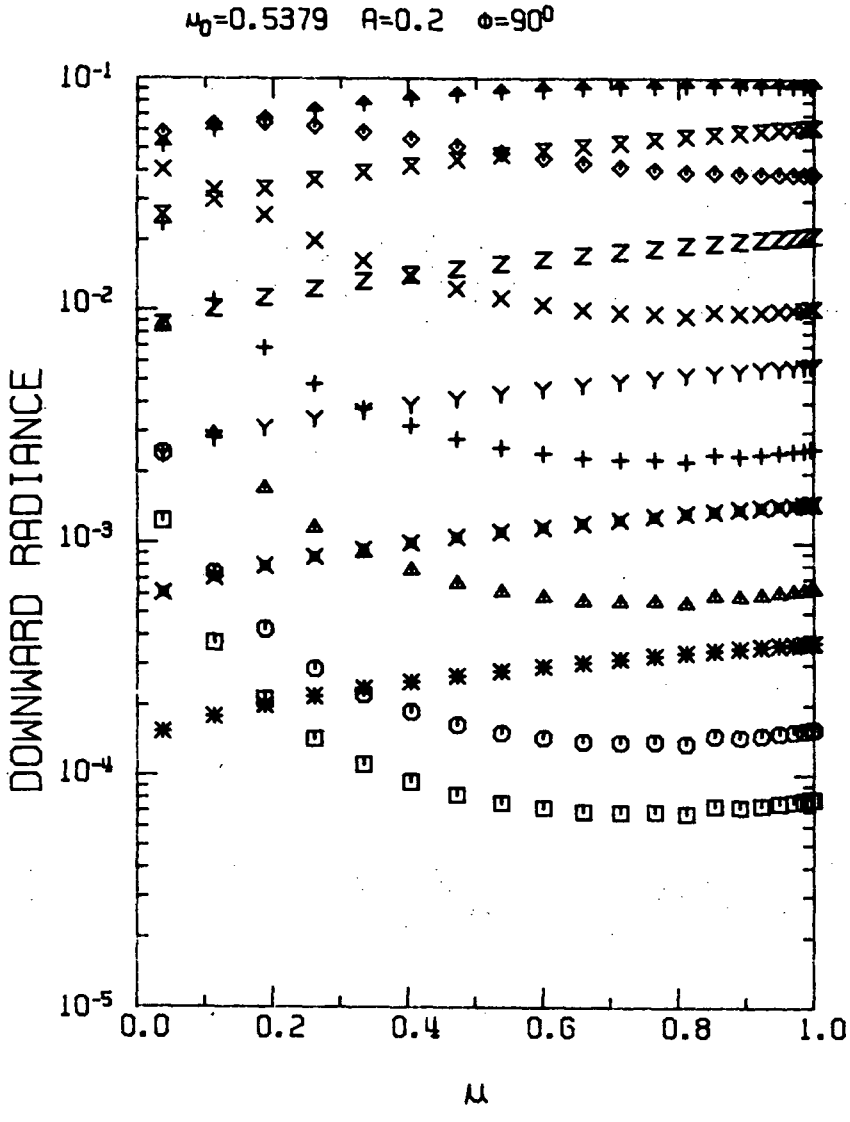
μ_0=0.5379 A=0.2 ϕ=90^0
DOWNWARD RADIANCE
10^{-1}
10^{-2}
10^{-3}
10^{-4}
10^{-5}
0.0
0.2
0.4
0.6
0.8
1.0
μ

a.

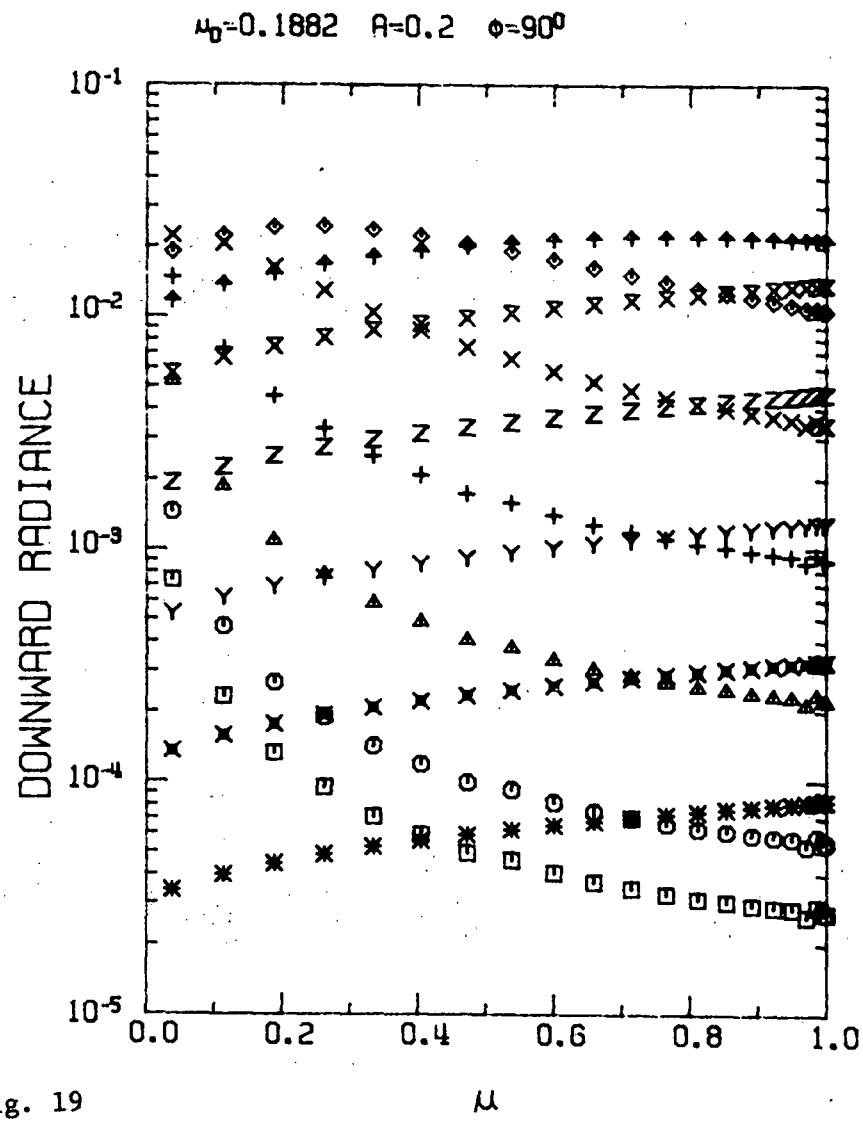
μ_0=0.1882 A=0.2 ϕ=90^0
DOWNWARD RADIANCE
10^{-1}
10^{-2}
10^{-3}
10^{-4}
10^{-5}
0.0
0.2
0.4
0.6
0.8
1.0
μ

b.

Fig. 19

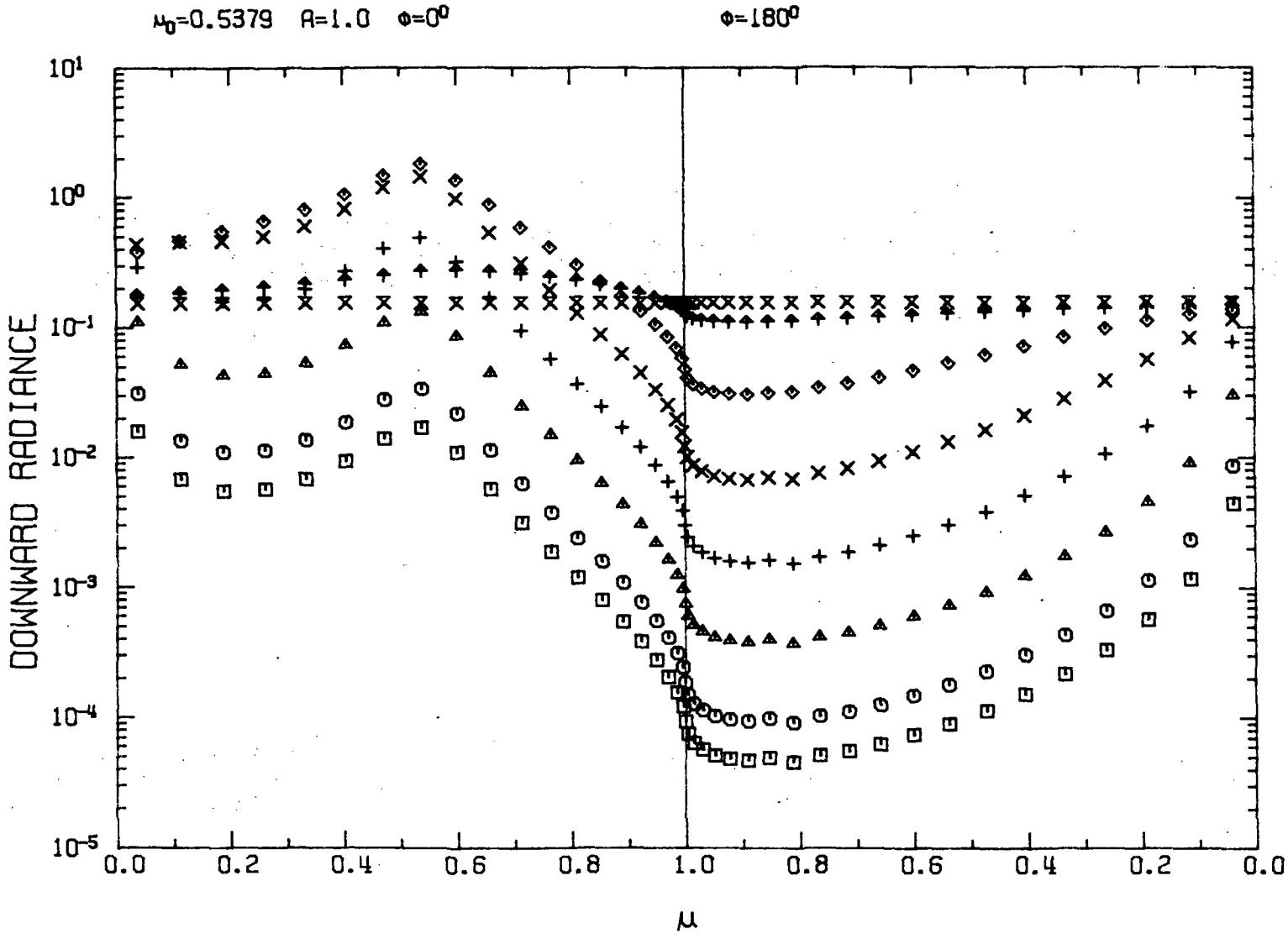
μ_0=0.5379 A=1.0 ϕ=0^0
ϕ=180^0
DOWNWARD RADIANCE
10^1
10^0
10^{-1}
10^{-2}
10^{-3}
10^{-4}
10^{-5}
0.0
0.2
0.4
0.6
0.8
1.0
0.8
0.6
0.4
0.2
0.0
μ

Fig. 20

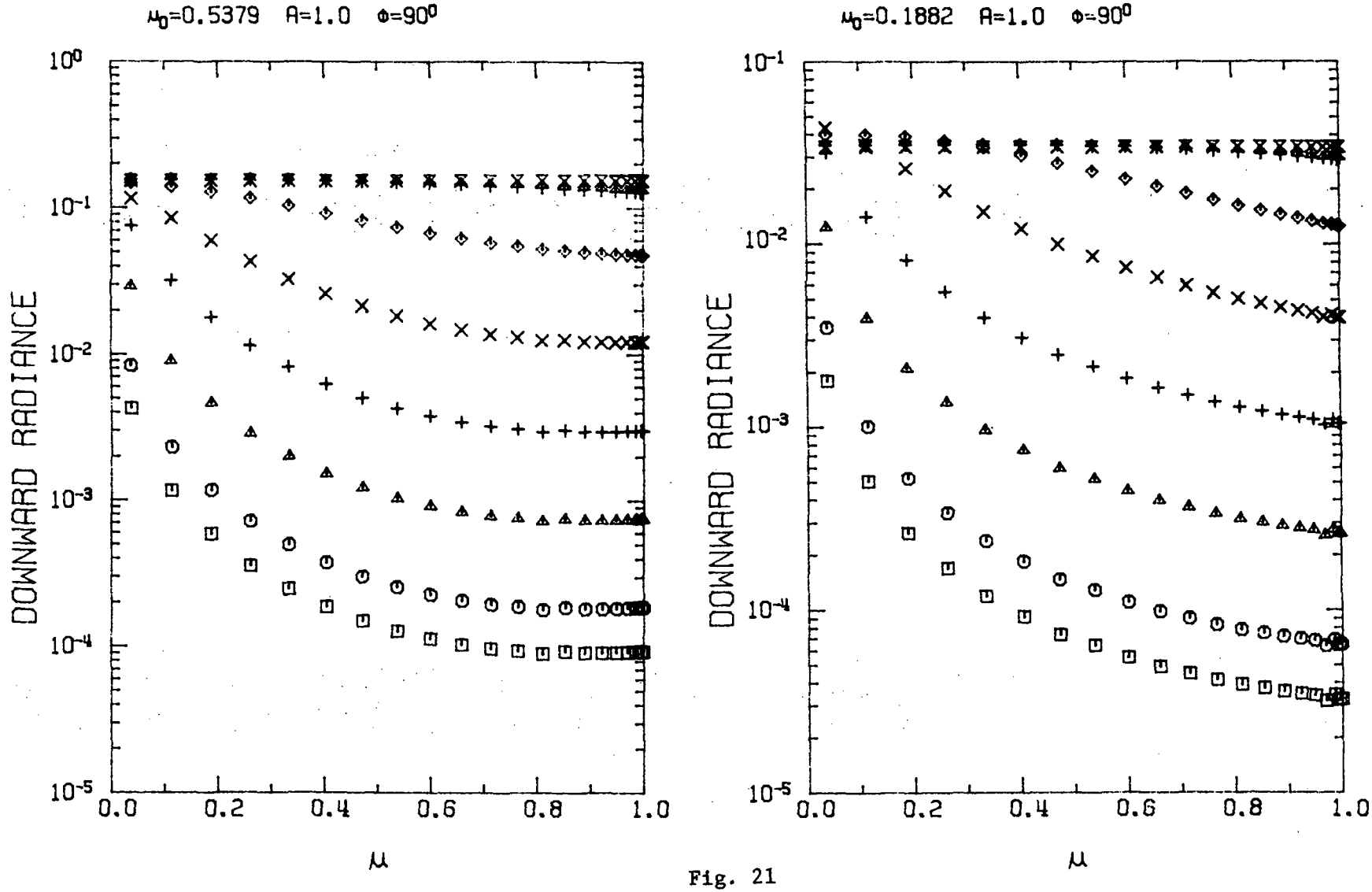
μ_0=0.5379 A=1.0 ϕ=90^0
DOWNWARD RADIANCE
10^0
10^{-1}
10^{-2}
10^{-3}
10^{-4}
10^{-5}
0.0
0.2
0.4
0.6
0.8
1.0
μ
μ_0=0.1882 A=1.0 ϕ=90^0
DOWNWARD RADIANCE
10^{-1}
10^{-2}
10^{-3}
10^{-4}
10^{-5}
0.0
0.2
0.4
0.6
0.8
1.0
μ

Fig. 21

a.

b.

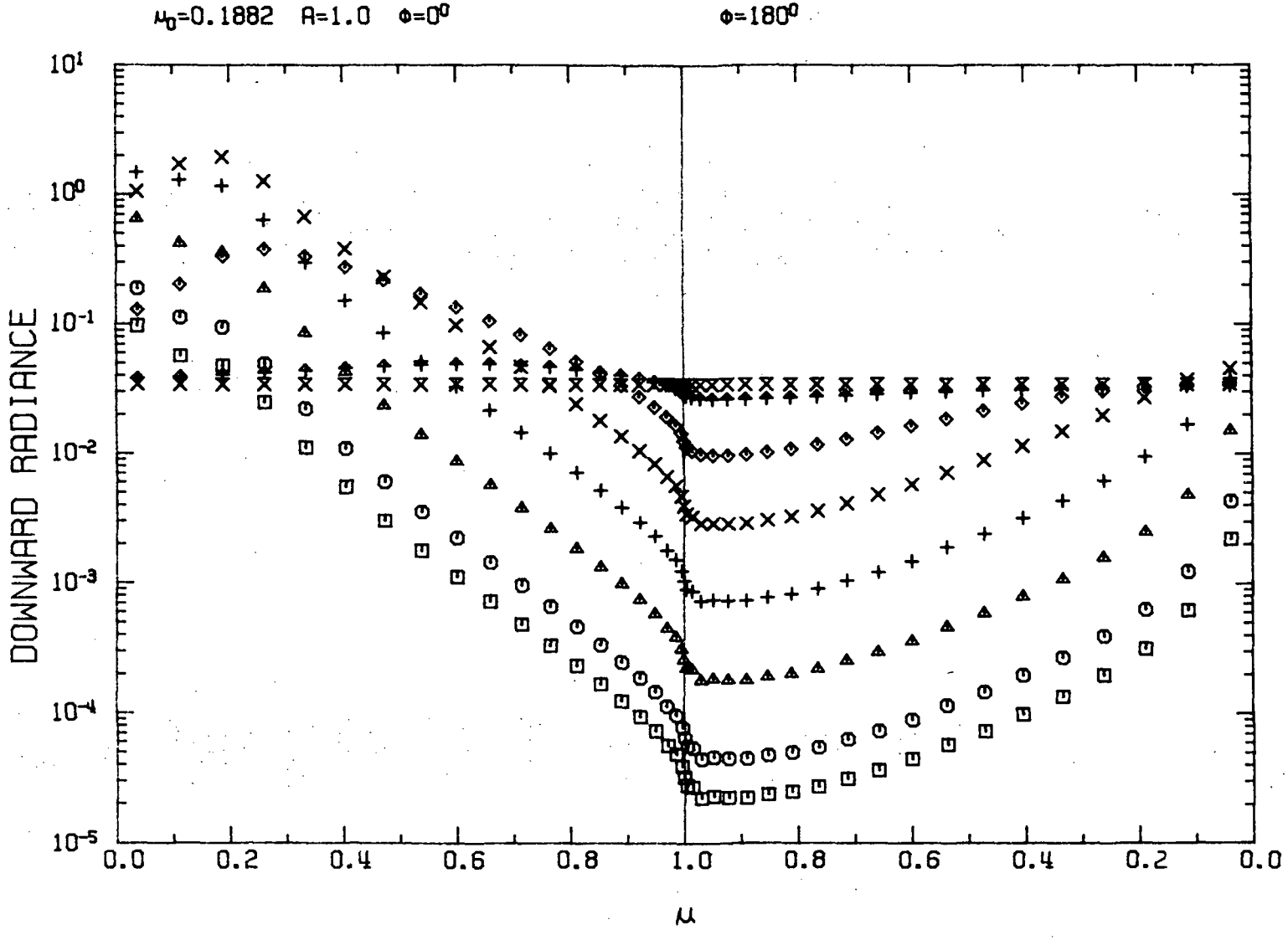
μ_0=0.1882 A=1.0 Φ=0°
Φ=180°
DOWNWARD RADIANCE
10^{1}
10^{0}
10^{-1}
10^{-2}
10^{-3}
10^{-4}
10^{-5}
0.0
0.2
0.4
0.6
0.8
1.0
0.8
0.6
0.4
0.2
0.0
μ

Fig. 22

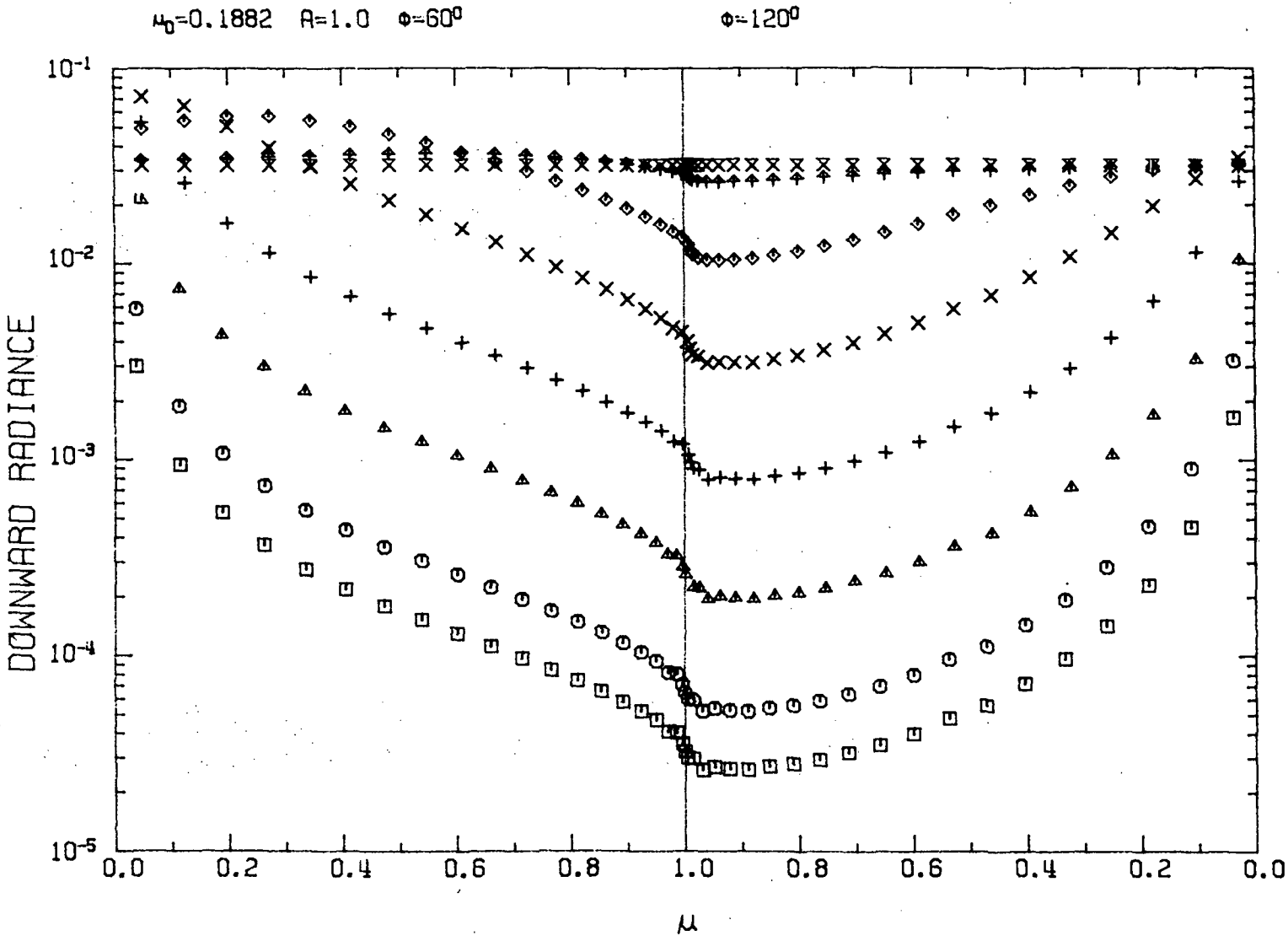
μ_0=0.1882 A=1.0 Φ=60°
Φ=120°
DOWNWARD RADIANCE
10^{-1}
10^{-2}
10^{-3}
10^{-4}
10^{-5}
0.0
0.2
0.4
0.6
0.8
1.0
0.8
0.6
0.4
0.2
0.0
μ

Fig. 23